Title

Potent, Selective, and Membrane Permeable 2-Amino-4-Substituted Pyridine-Based Neuronal Nitric Oxide Synthase Inhibitors.

Journal

Journal of medicinal and pharmaceutical chemistry, 66(14)

Authors

Vasu, Dhananjayan

Do, Ha

Li, Huiying

et al.

Publication Date

2023-07-27

DOI

10.1021/acs.jmedchem.3c00782

Peer reviewed

HHS Public Access

Author manuscript

J Med Chem. Author manuscript; available in PMC 2024 July 27.

Published in final edited form as:

J Med Chem. 2023 July 27; 66(14): 9934–9953. doi:10.1021/acs.jmedchem.3c00782.

Potent, Selective, and Membrane Permeable 2-Amino-4-Substituted Pyridine-Based Neuronal Nitric Oxide Synthase Inhibitors

Dhananjayan Vasu[†], **Ha T. Do**[†], **Huiying Li**[§], **Christine D. Hardy**[§], **Amardeep Awasthi**[†], **Thomas L. Poulos**[*,§], **Richard B. Silverman**[*,†,¶]

[†]Department of Chemistry, Department of Molecular Biosciences, Chemistry of Life Processes Institute, Center for Developmental Therapeutics, Northwestern University, 2145 Sheridan Road, Evanston, Illinois 60208-3113, United States

[¶]Department of Pharmacology, Feinberg School of Medicine, Northwestern University, Chicago, Illinois 60611, United States

[§]Departments of Molecular Biology and Biochemistry, Pharmaceutical Sciences, and Chemistry, University of California, Irvine, California 92697-3900, United States

Abstract

A series of potent, selective, and highly permeable human neuronal nitric oxide synthase inhibitors (hnNOS), based on a difluorobenzene ring linked to a 2-aminopyridine scaffold with different functionalities at the 4-position, is reported. In our efforts to develop novel nNOS inhibitors for the treatment of neurodegenerative diseases, we discovered **17**, which showed excellent potency toward both rat (K_i 15 nM) and human nNOS (K_i 19 nM), with 1075-fold selectivity over human eNOS and 115-fold selectivity over human iNOS. **17** also showed excellent permeability (P_e = 13.7 x 10^{-6} cm s^{-1}), a low efflux ratio (ER 0.48), along with good metabolic stability in mouse and human liver microsomes, with half-lives of 29 and > 60 minutes, respectively. X-ray co-crystal structures of inhibitors bound with three NOS enzymes, namely, rat nNOS, human nNOS, and human eNOS, revealed detailed structure-activity relationships for the observed potency, selectivity, and permeability properties of the inhibitors.

[*]Corresponding Authors: For R.B.S.: phone, +1 (847) 491-5653; fax: +1 (847) 491-7713; Agman@chem.northwestern.edu; For T.L.P.: phone, +1 (949) 824-7020; poulos@uci.edu.

Supporting Information

The Supporting Information is available free of charge at https://pubs.acs.org/doi/xxxxxx. Synthetic details and characterization for the key intermediates and the final compounds; copies of NMR spectra and HPLC traces for the final compounds; crystal structures of rat nNOS with compounds **16–21** and **23**, human nNOS with compounds **16–23**, and heNOS with compounds **16–23**; crystallographic data collection and refinement statistics for rat nNOS, human nNOS, and human eNOS; NOS enzyme inhibition assay; permeability assay; metabolic stability assay (PDF); molecular formula strings (CSV)

Accession Codes

PDB codes for X-ray structures described in this study are as follow: rnNOS-**16**, 8FG9; rnNOS-**17**, 8FGA; rnNOS H692F-**18**, 8FGV; rnNOS-**19**, 8FGB; rnNOS-**20**, 8FGC; rnNOS R349A-**21**, 8FGD; rnNOS R349A-**23**, 8FGE; hnNOS-**16**, 8FGF; hnNOS-**17**, 8FGG; hnNOS-**18**, 8FGH; hnNOS-**19**, 8FGI; hnNOS-**20**, 8FGJ; hnNOS-**21**, 8FGK; hnNOS-**22**, 8FGL; hnNOS-**23**, 8FGM; heNOS-**16**, 8FGN; heNOS-**17**, 8FGO; heNOS-**18**, 8FGP; heNOS-**19**, 8FGQ; heNOS-**20**, 8FGR; heNOS-**21**, 8FGS; heNOS-**22**, 8FGT; heNOS-**23**, 8FGU. Authors will release the atomic coordinates upon article publication.

The authors declare no competing financial interest.

Graphical Abstract

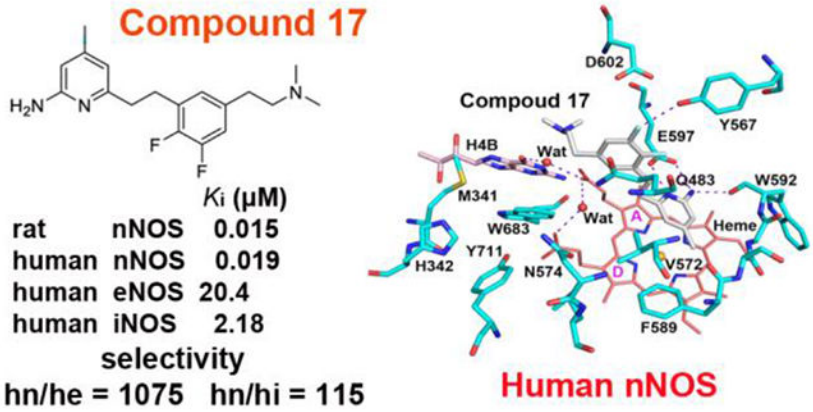

Introduction

Nitric oxide (NO) serves as an essential second messenger in human physiology.[1–2] The role of NO is unique: it regulates numerous essential processes such as neurotransmission,[3] smooth muscle relaxation,[4] vasodilation,[5] and the immune response.[6] In mammals, NO is produced endogenously by nitric oxide synthases (NOSs) via the oxidation of L-arginine to L-citrulline with the aid of NADPH and oxygen. NOSs exist in three isozymic forms in humans: neuronal NOS, inducible NOS, and endothelial NOS.[7] Neuronal NOS (nNOS) catalyzes the oxidation of L-arginine in the central nervous system (CNS) to produce NO, a critical neurotransmitter for neuronal communication.[8–10] Inducible NOS (iNOS) produces cytotoxic NO and assists in the immune response to destroy pathogens and microorganisms.[11] Endothelial NOS (eNOS) generates NO to reduce the blood pressure through the relaxation of smooth muscle.[12]

NO plays a key role in the mediation of neurodegeneration in numerous diseases of the nervous system.[13–15] Although the production of physiological levels[16] of NO by nNOS is beneficial for neuronal communication, its overproduction has been associated with the formation of extremely reactive species[17–19] such as peroxynitrite ($ONOO^-$) in the presence of superoxide. The highly oxidizing nature of the peroxynitrite causes excessive nitration and/or nitrosylation of proteins leading to their degradation and misfolding, particularly at high concentrations of NO.[20] nNOS has also been shown to be involved in several chronic neurodegenerative pathologies such as Alzheimer's disease (AD),[21] Parkinson's disease (PD),[22] Huntington's disease (HD),[23] amyotrophic lateral sclerosis (ALS),[24] chronic headaches,[25] and neuronal damage during stroke.[26]

NOSs are homodimeric enzymes with each NOS monomer containing a C-terminal reductase and an N-terminal oxygenase domain, separated by a flexible region where calmodulin binds when activated by calcium ions.[27] The reductase domain contains binding sites for flavin adenine dinucleotide (FAD), flavin mononucleotide (FMN), and reduced nicotinamide adenine dinucleotide phosphate (NADPH). The reductase domain is responsible for transporting electrons to the iron center of the heme during the biosynthesis

of NO, whereas the oxygenase domain contains binding sites for noncatalytic zinc (Zn^{2+}), tetrahydrobiopterin (H_4B), catalytic heme center, and the substrate, L-arginine.[7] In the active site, NOSs catalyze the oxidation of L-arginine to L-citrulline and release NO in the presence of NADPH and molecular oxygen. The crucial electron cascade reaction is initiated at the reductase domain by the two-electrons from NADPH, which pass through FAD and FMN. In the process, the enzyme undergoes a conformational change triggered by calmodulin binding that allows the electrons to pass from FMN to the iron center of heme in the oxygenase domain.[28]

Recent studies have indicated that inhibition of nNOS is promising for prevention and/or treatment of neuronal damage in animal models.[29] However, if nNOS inhibition is not sufficiently selective, inhibition of eNOS could result in hypertension and cardiovascular problems,[30] and iNOS inhibition could lead to immune defense failure.[31] Therefore, selective inhibition of nNOS over other isoforms is critical for the treatment of neurological disorders.[7,32–33] Because of the high similarity in the active site of all three NOS isoforms, achieving such a highly selective inhibition of one isoform over the others can be quite challenging. However, it is possible to exploit the subtle difference in and around the active site to develop highly selective nNOS inhibitors.[33] Any potential inhibitor must also be able to cross the blood-brain barrier for successful delivery into the brain, which is another common challenge in CNS drug discovery.[34–38]

There are several factors that can significantly improve blood-brain barrier permeability, as evidenced by the properties of successful CNS drugs.[34–35,39] These include: low molecular weight (MW < 500 Da; preferably 350-400 Da); high lipophilicity (preferably ClogP < 5); low topological polar surface area (TPSA < 76 $Å^2$; preferably 25-60 $Å^2$); the number of hydrogen bond donors, both OH and NH_2 (HBD = 5; preferably 3); the number of hydrogen bond acceptors, both O and N atoms (HBA = 10; preferably 7); a reduced number of rotatable bonds (RB < 8; preferably 4-5); reduced p*K*a of basic amino groups (p*K*a 7.5-10.5; preferably 8.4); and reduced P-glycoprotein (P-gp) efflux (ER < 2).[40]

Our laboratory has been devoted to the development of selective nNOS inhibitors that have excellent potency while retaining high isoform selectivity and blood-brain barrier (BBB) permeability.[27,40–44] Several medicinal chemistry approaches have been used to improve the pharmacokinetic properties of nNOS inhibitors. For example, introducing a bis-2-aminopyridine pharmacophore (**1**),[45] pharmacophore replacement (**2**),[46] incorporation of intramolecular hydrogen bonds (**3**),[50] modulating amine basicity (**4**),[48] prodrug conversion (**5**),[49] incorporation of a pyridine linker (**6**),[47] exchanging the pyridine linker with monofluoroaryl (**7**),[42] disconnecting fluoroaryl linkers (**8**),[40] and exchanging the pyridine linker with difluoroaryl (**9**),[44] have resulted in considerable improvements in the pharmacokinetic properties of NOS inhibitors as represented in Figure 1.

Our efforts to achieve nNOS inhibitors with excellent potency and isoform selectivity have led to a promising class of molecules based on the 2-aminopyridine scaffold. The first generation of these molecules, such as 2-aminopyridine with a pyridine linker (**6**), however, showed little or no permeability in a Caco-2 assay, a model for BBB permeation.[50] Molecules in the second generation, modified by exchanging the pyridine linker with mono-

or difluorobenzene rings (**7** and **9**),[42,44] respectively, showed a significant improvement in permeability while maintaining high inhibitory activity. For example, **7** displayed good potency and excellent isoform selectivity for human nNOS ($K_{i\ (hnNOS)}$ = 30 nM; K_i (hnNOS)/K_i (heNOS) or hn/he = 2799). However, its high efflux ratio (ER = 5.9) in the Caco-2 permeability assay indicated it was a substrate for P-glycoprotein or other active transport systems, which is unfavorable for CNS drug development.[42,44] Compound **8**, with a reduced number of rotatable bonds obtained by disconnecting the fluorobenzene linker, showed good potency for rat (K_i = 46 nM) and human nNOS (K_i = 48 nM) with high membrane permeability (P_e = 17.3 x 10^{-6} cm s^{-1}); but unfortunately, it had only moderate isoform selectivity (hn/he = 388; K_i (hnNOS)/K_i (hiNOS) or hn/hi = 135).[40] Compound **9**, with a difluorobenzene ring and an azetidine tail, demonstrated good inhibition for human nNOS (K_i = 23 nM) as well as its isoform selectivity (hn/he = 956; hn/hi = 77) and excellent brain permeability in the PAMPA-BBB assay (P_e = 16.3 x 10^{-6} cm s^{-1}) as well as Caco-2 (P_{app} = 17.0 x 10^{-6} cm s^{-1}) permeability assays. It also exhibited a low efflux ratio (ER = 0.8) in a Caco-2 bidirectional permeability assay, a desirable property for further development.[44]

In this work, using **9** as the lead compound, we investigated the effect of different steric and electronic changes at the 2-aminopyridine head of potential nNOS inhibitors by substituting various functionalities ranging from electron-withdrawing to electron-donating groups. We present our optimization of a series of potent, selective, and highly permeable human nNOS inhibitors based on **9**, having different substituents at the 4-position. The syntheses are much simpler compared to previous analogues that required protection and deprotection of the 2-aminopyridine head. The aim was to further improve cell-membrane permeability, reduce P-glycoprotein and BCRP substrate liability, and maintain potency and isoform selectivity.

In earlier reports, we demonstrated that the 2-aminopyridine scaffold was crucial for establishing interactions of those nNOS inhibitors with Glu-592 and Glu-597 at the active sites of both rat nNOS and human nNOS,[40–42,44,50] respectively, and that the installation of a lipophilic methyl group at the 4-position of the 2-aminopyridine improved potency and isoform selectivity.[51] Based on recent X-ray crystallographic analyses and the above experimental observations, we designed several structural modifications to lead **9**, focusing on exploring the effect of different steric and electronic modifications at the pyridine head, as well as exploring the structural diversity of the tail amino functionality and testing the effects of changing rigidity in the linker region between the 2-aminopyridine and difluorobenzene rings (Figure 2).

Different approaches that include modification of the rigidity, reduction in the number of rotatable bonds by truncation, bioisosteric replacement,[52–54] enhancement of lipophilicity, and modulation of the p*K*a of the amine nitrogen at the pyridine head, have been conducted to investigate their effects on the biological activity. To increase the rigidity within the molecule, reduce the p*K*a of the pyridine ring, and reduce the rotatable bonds, unsaturation (**10-14**) was installed between the 2-aminopyridine head and the difluorobenzene linker; the number of rotatable bonds also was reduced by shortening the tail amine chain length (**10, 13, 15**). Conversion of unsaturated bonds to saturated bonds enhanced flexibility (**15-18**) as well as pyridine basicity. Bioisosteric replacements of the 4-methyl group on

the 2-aminopyridine ring with 4-chloro (**12**), 4-methoxyl (**18**), 4-difluoromethyl (**23**), and 4-trifluoromethyl (**24**) and of the ring 3-C-H with N (**19**) were carried out with the aim of maintaining potency while optimizing additional properties, such as metabolic stability, cell-membrane permeability, solubility, and possibly toxicity.[52] To improve permeability, enhancement of lipophilicity was achieved by modifying the aliphatic groups at the tail amino group (**20**-**22**). Finally, modulation of amine basicity of the 2-aminopyridine, as well as maximization of the lipophilicity to improve permeability further within the molecule, was accomplished by substitution of the 4-methyl group with 4-CF_2H and 4-CF_3 groups **(23** and **24).**

Results and Discussion

Chemical Synthesis of the nNOS Inhibitors

The general synthetic route to inhibitors **10**-**11**, **13**-**15**, **17**, and **20**-**22** is outlined in Scheme 1. The linker difluorobenzene with different amine tail chains (**29**-**31, 35**, and **42**) was accessed from commercially available carboxylic acid **25** through the formation of benzyl alcohol **26** by reduction with BH_3. Compound **27** can be prepared by the Appel reaction of **26** in excellent yield. Cyanation of the corresponding benzyl bromide (**27**) and reduction with BH_3 gave the desired one-carbon extension of the chain and amine installation (**29**). The reductive amination of **29** with paraformaldehyde or acetaldehyde provided **30** and **31**, respectively, in excellent yields. Compound **35** was prepared from benzyl alcohol (**26**) by Swern oxidation and followed by Wittig reaction, giving the enol-ether (**33**), which was then cleaved to the aldehyde (**34**) upon treatment with TMSCl and KI.[55] The reductive amination of aldehyde **34** with *N*-methylpiperazine gave **35** in good yield. Compound **42** was prepared by the S_N2 substitution of benzyl bromide **27** with dimethylamine in an ethereal solution. After preparing the linkers (**29**-**31, 35**, and **42**), we focused on the synthesis of alkyne precursor **38**, starting from commercially available 2-amino-4-methyl-6-bromopyridine (**36**), which was allowed to react with trimethylsilylacetylene by a Sonogashira cross-coupling reaction.[40] Base-mediated TMS-deprotection (**37**) to alkyne precursor **38** went smoothly at room temperature. The crucial Sonogashira cross-coupling reaction between alkyne **38** and bromoaryls **29**-**31**, **35**, and **42** installed the internal alkyne into **10, 11**, and **39**-**41** successfully, which were converted to the flexible alkane products (**15**, **17**, and **20**-**22**) by hydrogenation with H_2, Pd/C as well as to the less flexible alkene products (**13**-**14**) by $LiAlH_4$ reduction.[56]

The synthetic route to **12** and **16** is outlined in Scheme 2. The Sonogashira cross-coupling reaction between 2-amino-4,6-dichloropyridine (**43**) and trimethylsilylacetylene was carried out at 120 °C under an inert atmosphere to obtain the corresponding coupled product (**44**) in a 79% yield. The desilylation with basic conditions gave the alkyne precursor (**45**) in 98% yield. The Sonogashira cross-coupling reaction between **45** and **30** furnished **12** in 65% yield. Our initial goal was to make the 4-chloro substitution at the 2-aminopyridine head under hydrogenation conditions (H_2, Pd/C, CH_3OH) at room temperature. However, this provided only the dechlorinated product (**16**) with the formation of only a trace amount of desired product.

The synthesis of **18** is outlined in Scheme 3, starting with 2,6-dichloro-4-hydroxy pyridine (**46**). *O*-Alkylation was achieved by a combination of excess K_2CO_3 and $(CH_3)_2SO_4$ followed by S_NAr benzylation, which led to **48** in a moderate yield. The Sonogashira reaction and desilylation gave alkyne precursor **50** in excellent yield. Compound **50** was then converted to an internal alkyne (**51**) by reaction with **30** under Sonogashira reaction conditions, which was further reduced to **52** with Pd/C and H_2. The debenzylation of **52** was achieved under strongly acidic conditions to provide **18**.[57]

The general synthetic route to **19** is outlined in Scheme 4. In brief, the alkyne precursor (**54**) was accessed from **30** with trimethylsilylacetylene under palladium catalysis and subsequent desilylation conditions. Iodo species **56** is prepared from commercially available 2-amino-4-chloro-6-methylpyrimidine (**55**) with iodotrimethylsilane under refluxing conditions.[58] **54** was coupled with the iodo species (**56**) under Sonogashira reaction conditions at 25 °C to give the internal alkyne (**57**) in 75% yield. Finally, **57** was converted to the final product (**19**) by hydrogenation with Pd/C at room temperature.

The synthetic approaches to compounds **23** and **24** are outlined in Schemes 5 and 6, respectively. Alkyne precursor **61** was prepared in an excellent yield from commercially available 2,6-dichloro-4-(difluoromethyl)pyridine (**58**) through S_NAr benzylation and Sonogashira coupling,[40] followed by base mediated desilylation. The Sonogashira cross-coupling of **61** with **30** provided the internal alkyne (**62**) in 68% yield, which was further reduced to **63** by hydrogenation. The cleavage of the 4-methoxybenzyl protection group[59] was achieved by treating **63** with TFA at 80 °C, which gave **23** in 85% yield. Compound **24** was prepared in a similar manner to that described for **23** with slight modifications, including: (i) microwave assisted Sonogashira cross-coupling reactions[60] (**65** to **66, 67** to **68**), and (ii) cleavage of the 4-methoxybenzyl protection (**68** to **69**) before the final hydrogenation (**69** to **24**) reaction. The order of hydrogenation and amine deprotection in Scheme 5 was reversed in Scheme 6 because the Sonogashira cross coupling in the latter scheme led to some deprotection of the amine; consequently, the amine was deprotected first to avoid having to separate protected (**68**) and unprotected (**69**) prior to hydrogenation.

Biochemical Activity of the nNOS Inhibitors

All nNOS inhibitors (**10-24**) were converted to the HCl salt form prior to assay. The potency and selectivity of new NOS inhibitors were determined using the NO hemoglobin (Hb) capture assay[61] using L-arginine (NO donor) and NOS inhibitor (inhibitor of NO formation) as positive and negative controls, respectively,[71] and the results are summarized in Table 1.

All compounds were assayed with purified rat nNOS to test their inhibitory activity (K_i). The most promising inhibitors were selected for further assays using human nNOS, human iNOS, and human eNOS for evaluation of potency as well as isoform selectivity. Selected inhibitors were chosen for evaluation using additional assays, including the PAMPA–BBB assay to assess cell-membrane permeability, the Caco-2 bidirectional assay to gauge P-gp and BCRP substrate liability, and microsomal stability assays to evaluate metabolic stability. The ratio, hnNOS/rnNOS (hn/rn), is defined as the ratio of the K_i values of the inhibitors for human and rat nNOS. The hn/rn ratio is important for evaluating the potential translation of

these inhibitors from preclinical to clinical studies. Isoform selectivity for human nNOS over human iNOS (hn/hi) and eNOS (hn/he) was obtained by comparing the K_i values of human nNOS with human iNOS and human eNOS, respectively.

Initial screening of the new compounds was carried out using rnNOS to test their inhibitory activities. Structure–activity relationship (SAR) studies of compounds **10**-**14** revealed that the unsaturated bond between the 2-aminopyridine head and the difluorobenzene linker, which enhances the rigidity within the molecule considerably, decreased their inhibitory activities. For example, the shorter amine tail with alkyne compound **10** ($K_{i\ rnNOS}$ = 392 nM) underperformed in terms of potency as compared to its extended version (**11**, $K_{i\ rnNOS}$ = 293 nM). About 2- to 3-fold improved inhibitory activity was observed for alkene derivatives (**13, 14**) regardless of the chain length of their amine tails.

Bioisosteric replacement is a powerful tool for modulating drug-like properties, toxicity, and chemical space of experimental therapeutics.[54] The chlorine atom is considered to be isosteric and isolipophilic with a methyl group and is very often selected as a bioisosteric replacement to increase metabolic stability.[52–53,62] The bioisosteric replacement of the 4-methyl group (**11**) with a 4-chloro group might improve its bioavailability; however, it decreased the potency (**12**, $K_{i\ rnNOS}$ = 1995 nM). In fact, all the compounds with the unsaturated linker between the two aromatic rings (**10**-**14**) exhibited rather poor potency.

Next, we focused our attention on the synthesis of highly flexible alkanes such as **15**-**24** by hydrogenating the appropriate alkynes and testing their inhibitory activities. As anticipated, the flexible alkane (**15**, K_i rnNOS = 91 nM) showed better performance over its rigid counterparts (**10** or **13**), encouraging further lead optimization. Interestingly, chain elongation of **15**, i.e., the lengthening of the amine tail by one carbon while retaining a 4-methyl substituent at the 2-aminopyridine ring (**17**), showed excellent potency for rat (K_i = 15 nM) and human nNOS (K_i = 19 nM), with 1075-fold human eNOS and 115-fold human iNOS selectivity (indicated in bold in Table 1). This result suggests that a lipophilic alkyl group, such as the 4-methyl group, is the best substituent for this position, likely because of its favorable hydrophobic interactions with the side chains of Phe584 and Val567 and the backbone of Ser585 in rnNOS within a pocket of limited size.[51] The lack of this 4-methyl group in **16** as compared to **17**, resulted in a dramatic drop in potency, presumably because of a loss in favorable hydrophobic interactions with the nearby lipophilic residues. Incorporation of perfluorinated alkyl fragments such as 4-CF_2H (**23**) and 4-CF_3 (**24**) typically increases the lipophilicity (log *P*)[63] within the molecule; however, due to the electron-withdrawing nature of these groups, it also considerably reduces potency most likely due to the basicity of the 2-aminopyridine head, thereby weakening the crucial H-bonding interactions with Glu592, even though they are the best lipophilic substituents other than the 4-methyl group.

Pharmacophore replacement of the 2-aminopyridine group with 2-aminopyrimidine (**19**, $K_{i\ rnNOS}$ = 6577 nM) was achieved by bioisosteric replacement of the ring ‘C-H’ atoms with a ring ‘N’ atom at the C3 position of the 2-aminopyridine scaffold of lead **9**.[64–65] Such an apparently subtle change to a 2-aminopyrimidine in **19** as compared to 2-aminopyridine in **17** resulted in a 438-fold loss in potency. We expected that exchanging the 4-methyl

group with a strong electron-donating substituent, such as a 4-methoxyl group (**18**), might increase the basicity of the 2-aminopyridine head, thereby enhancing potency. But the results revealed that it decreased potency by 5-fold as compared to **17**. We also observed that the electron-withdrawing fluorinated alkyl species (**23, 24**) were not as potent as the 4-methyl derivative (**17**) in this study.

Finally, we focused on functionalizing the amine tail by increasing lipophilic aliphatic groups (**17** and **20**-**22**) while retaining the 4-methyl substituent at the 2-aminopyridine head to improve its isoform selectivity and permeability and hopefully maintaining its potency. We found that the steric bulk on the amine tail plays a crucial role in determining isoform selectivity. As discussed earlier, **17**, with an *N*, *N*-dimethylamino tail group, exhibits excellent potency and selectivity, whereas the primary amine derivative **20** showed weaker potency and poor iNOS selectivity. The highly bulky *N*, *N*-diethyl amine tail derivative (**21**) showed good potency and isoform selectivity but less than that observed with **17**. Compound **22**, with an *N*-methylpiperazine tail, had lower potency with both rat and human nNOS and showed improved potency with heNOS, leading to poorer hn/he selectivity.

Assessment of Permeability of the nNOS Inhibitors

A set of highly active inhibitors (**10**-**12** and **16**-**24**) was selected and tested for their potential BBB permeability using the PAMPA-BBB assay (Table 2). Primary amine **20** performed well in the PAMPA-BBB assay, displaying good permeability (P_e = 12.6 x 10^{-6} cm s^{-1}). Compound **10** showed the highest permeability (P_e = 26.8 x 10^{-6} cm s^{-1}) in this series, likely due to the presence of both a rigid alkyne as well as lipophilic alkyl substituents in the amine functionality. Compound **21**, with an *N*, *N*-diethyl amine tail, showed the next highest permeability (P_e = 17.6 x 10^{-6} cm s^{-1}) because of the presence of its highly lipophilic alkyl substituents. Similarly, the lipophilic tertiary amine **17** (P_e = 13.7 x 10^{-6} cm s^{-1}) also displayed higher effective permeability over its primary amine variant (**20**). Compound **11** with a rigid alkyne and lipophilic tertiary amino functionality exhibited higher permeability over its alkane version (**17**). The absence of a methyl group at the 4-position on the 2-aminopyridine head (**16**) slightly reduced the P_e value by two orders of magnitude as compared to **17** but was comparable to **12**. A piperazine tail (**22**), containing two tertiary amines in the skeleton, decreased permeability by three orders of magnitude over parent **17**. We also found that exchanging hydrogen atoms with fluorine atoms in the 4-methyl substituent of the 2-aminopyridine head (**23, 24**) considerably increased the permeability of the NOS inhibitors (**23**, P_e = 16.0 x 10^{-6} cm s^{-1}; **24**, P_e = 17.3 x 10^{-6} cm s^{-1}). Notably, pyrimidine **19** (P_e = 11.7 x 10^{-6} cm s^{-1}), showed decreased permeability relative to **17**. On the other hand, the 4-methoxyl variant, **18**, exhibited moderate permeability in this series, likely due to increased polarity.

Based on the PAMPA-BBB results, the magnitude of permeability of 4-pyridyl substituents is in the following order: (4-CF_3 (**24**) > 4-CF_2H (**23**) > 4-CH_3 (**17**) > 4-H (**16**) ~ 4-Cl (**12**) > 4-OCH_3 (**18**). Notably, the hydrophobic interactions of the 4-CF_3 (**24**) substituent enhances compound permeability by ~4 units relative to its parent 4-CH_3 substituent (**17**) in this assay.

Assessment of the Efflux Transporter Liability of the nNOS Inhibitors

Because of its high inhibitory activity and excellent PAMPA-BBB assay permeability (Tables 1 and 2), **17** was selected for further studies to test its potential BBB permeability compared to older molecules **7** and **9** using the Caco-2 bidirectional permeability assay (Table 3). The blood-brain barrier is located at the interface of the blood vessels and brain tissues and is formed by brain capillary endothelial cells creating a tight junction to protect the brain from circulating xenobiotic molecules. P-glycoprotein (P-gp) and breast-cancer-resistant protein (BCRP) are two important ATP-driven efflux transporters responsible for removing xenobiotic molecules, including drugs, from the brain and are highly expressed in the region of the blood-brain barrier.[67–68] P-gp has a larger substrate specificity and therefore has higher significance over BCRP in CNS drug discovery.[38] The substrate liability of a compound for these transporters can be evaluated based on the efflux ratio (ER) obtained from a Caco-2 bidirectional permeability assay.[69] This assay measures the capacity of compounds to cross a monolayer of colon cells with expressed P-gp and BCRP from two directions, either from apical to basal (A → B) or from basal to apical (B → A) direction.[42,44,46,70] The efflux ratio is calculated based on the ratio of the apparent permeability (P_{app}) of B → A over A → B. Compounds with an efflux ratio ≥ 3 are considered to be substrates of P-gp and BCRP, leading to limited retention in the brain.[35] Compound **7** has a high efflux ratio (ER = 5.9) and is, therefore, a strong substrate for P-gp and hence not considered a good candidate as a CNS drug. Compound **17**, however, has a significantly low P-gp and BCRP substrate liability as indicated by its low efflux ratio (ER = 0.48), lower than lead **9** (ER = 0.8) and the highly CNS permeable control, metoprolol (ER = 0.55). Taken together, these results indicate that **17** is a good candidate for a CNS drug discovery program.

Metabolic Stability of the nNOS inhibitors

Enhancing the lipophilicity of nNOS inhibitors to improve their permeability may cause a negative effect on their metabolic stability. Therefore, we further investigated the metabolic stability of lead compound **9** and **17** in mouse (MLM) and human liver microsomes (HLM). Terfenadine and imipramine were used as positive controls for HLM and MLM, respectively. The results indicated that both **9** and **17** have moderate stability in MLM with their half-life ($t_{1/2}$) of 16 and 29 minutes, respectively. Our newly designed compound **17** is approximately 2-fold more stable than the previous lead **9**. In HLM, in contrast, both compounds displayed very good stability with their half-life more than 60 minutes.

Exploration of Structure-Activity Relationships of the nNOS Inhibitors using Crystal Structures of Bound Compounds

Effects of rigidifying lead compound 9 (12)—To further evaluate the SAR of the nNOS inhibitors, we generated crystal structures of selected compounds bound to the heme domain of rnNOS, hnNOS, and heNOS, which contain the enzyme active site. First, we examined the effects of rigidifying the linker between 2-aminopyridine and difluorobenzene that had led to improved membrane permeability (Table 2). However, the poor inhibitory potency of **10**-**14** with rnNOS prevented us from pursuing structural analysis of these compounds, except for **12.**

Due to poor potency (Table 1) we were unable to obtain much detail from the crystal structure of the rnNOS-**12** complex. Density around **12** is only available for the 2-aminopyridine and the rigid linker, with the remainder of inhibitor being disordered. Although the density quality prevented a full refinement, some features in the initially calculated density are worth discussing. We were curious about whether 4-Cl substitution on the 2-aminopyridine in **12** could be accommodated in the NOS active site. As shown in Figure S1, the bulky 4-Cl does fit in the active site of rnNOS, establishing a weak H-bond with the backbone amide N atom of Gly586. The two N atoms of the 2-aminopyridine in **12** can also H-bond with Glu592 as seen with other 2-aminopyridine based inhibitors.[40,42] The main difficulty for **12** in binding to rnNOS is that the rigid linker places the difluorobenzene in an awkward position where it may easily clash with the heme propionates. The crystal structure indicates that the orientation of the difluorobenzene is highly uncertain (Figure S1). In contrast, for compounds with a flexible linker, as in **17**, steric clashes can be avoided (see below). Compounds **10, 11** and **13, 14** might have similar issues as we see with **12** in terms of the clashes. Indeed, in our previous work on a series of 2-aminopyridine compounds shortened by removing the difluorobenzene linker entirely, such as **8** in Figure 1, inhibitors with a rigidified chain caused poor potency compared to their counterpart with a flexible chain.[40] This dilemma is repeated here, with the reduction of rotatable bonds intended to improve membrane permeability causing poor inhibitory potency.

Effects of enhancing the flexibility of nNOS inhibitors (16-18)—Next, we examined the effects of changing rigid alkynes to flexible alkanes as the linker between the 2-aminopyridine and the difluorobenzene moieties in **16-18**, with variations at the 4-position of the 2-aminopyridine. Compounds **16** and **17** resemble each other except for the 4-substituent on the 2-aminopyridine. The binding modes of **16** and **17** to either the rnNOS or the hnNOS active site are similar. Briefly, **16** and **17** adopt a bent-back mode in rnNOS with the 2-aminopyridine anchoring to Glu592 in rnNOS or Glu597 in hnNOS (Figures 3A and 3B, respectively), and the difluorobenzene bending back toward the heme plane forcing propionate D into a downward conformation. The tail amine approaches a water molecule sitting between the H_4B and propionate A.

In contrast, **16** and **17** show an upward binding mode in hnNOS, with the difluorobenzene close to Tyr567 for an H-bond (Figures 4A and 4B). This upward difluorobenzene position forces the Gln483 side chain to an alternate rotamer conformation. Binding of **16** to hnNOS also exhibits an alternative bent-back conformation in one of the two subunits observed in the hnNOS-**16** structure (Figure 4A, light-pink inhibitor backbone). The tail amine in the upward binding mode also approaches the water in between H_4B and propionate A. These totally different binding preferences, bent-back for rnNOS and upward for hnNOS, were also observed in our previous studies.[42]

Interestingly, the potency values with rnNOS and hnNOS for **16** and **17** are starkly different, with **16** being a rather poor inhibitor of rnNOS and hnNOS and **17** having excellent potency against these two enzymes. The similar binding modes of **16** and **17** to rnNOS and hnNOS implies that the sole reason for **16** being a poor inhibitor is its lack of the 4-methyl group on 2-aminopyridine. The anchoring force of the 2-aminopyridine is derived from

its bifurcated H-bonds with the active site Glu residue (Glu592 in rnNOS and Glu597 in hnNOS). Although missing a 4-methyl group does not alter hydrogen bonding to the active site Glu in nNOS, lack of the hydrophobic interactions with Val567 and Phe584 (rnNOS) or Val572 and Phe589 (hnNOS) that the 4-methyl group establishes in the small nonpolar pocket enclosing the active site apparently does cause significant loss in binding affinity.

The binding of **16** and **17** to heNOS shows important differences as compared to their binding to rnNOS and hnNOS. While the 2-aminopyridine position was well resolved in density maps for **16** and **17**, disordering was observed for the remainder of both inhibitors. Figure 5 displays some choppy density in the region outside of the 2-aminopyridine. The difluorobenzene of **16** is like a roof covering both propionates with its F atoms pointing sideways to Met399 (Figure 5A). In sharp contrast, the same ring in **17** locates almost vertically between two propionates with the F atoms pointing up toward Gln247 for an H-bond (Figure 5B). Although the electron density is weak, the difluorobenzene of **17** in heNOS adopts the less favorable “vertical” position and not the favorable upward position observed in hnNOS. The two different orientations of the difluorobenzene for **16** and **17** in heNOS position the tail amine to entirely different locations in the two structures (Figures 5A and 5B). Based on the 2.5-fold better K_i value of **17** over **16** (Table 1) with heNOS, the difluorobenzene vertical orientation (relative to the heme plane) in **17** might be more favorable than the horizontal one in **16**. The missing 4-methyl group in **16** could also account for some of the loss in binding affinity with heNOS.

To summarize, **17**, the best inhibitor in this series in terms of potency, isoform selectivity, and membrane permeability, displays two different binding modes in rnNOS and hnNOS. Nevertheless, the potency of **17** is similar for rnNOS and hnNOS because each of the modes, bent-back (Figure 3B) or upward (Figure 4B), has its own set of favorable enzyme-inhibitor interactions resulting in good binding affinity for both. Many of these binding interactions are absent in the heNOS-**17** structure (Figure 5B), especially the favorable position for the difluorobenzene, either the bent-back mode in rnNOS or the upward mode in hnNOS, which are replaced instead with a presumably less favorable positioning of the difluorobenzene and tail amine groups.

Introduction of a 4-methoxyl group in **18** was carried out to adjust the basicity of the 2-aminopyridine, but it also caused large structural changes in the enzyme-inhibitor interactions (Figure 6). The 4-methoxyl group is accommodated in the rnNOS active site, with the methoxyl oxygen atom making an H-bond with the backbone amide nitrogen atom of Gly586 (Figure 6A). The two H-bonds from the 2-aminopyridine to Glu592 are unaltered. The difluorobenzene of **18** adopts an unusual upward binding mode in this rnNOS-**18** structure (Figure 6A). This upward mode is like that seen more frequently for inhibitors in hnNOS structures but with some subtle differences. The hnNOS-**18** structure shown in Figure 6B is the typical upward binding mode in hnNOS, where one of the F atoms of the difluorobenzene H-bonds with Tyr567. In contrast, it is Tyr588 in rnNOS that donates an H-bond to the F atom of difluorobenzene. In hnNOS, the residue equivalent to Tyr588 of rnNOS is Tyr593, while Tyr562 of rnNOS corresponds to Tyr567 in hnNOS (compare panel A and B in Figure 6). Although the H-bonding partner is a different Tyr residue in the two nNOS structures, the similar K_i values for **18** in rnNOS and hnNOS are supported by the

two structures. The binding mode of **18** in heNOS is like that observed for **16** (Figure 5A). That is, the ethylene linker from the 2-aminopyridine brings the difluorobenzene upward covering both propionates, with its two F atoms facing toward Met339 (Figure 6C). The tail amine of **18** directly interacts with propionate A in heNOS, which is rarely observed in NOS-inhibitor structures. Taken together, these structures support the idea that bearing a 4-methyl group on the 2-aminopyridine affords **18** good inhibitor potency for nNOSs.

Effects of isosteric replacement in nNOS inhibitor 19—Although the change from a 2-aminopyridine in **17** to a 2-aminopyrimidine in **19** is subtle, it results in a large difference in inhibitor potency (Table 1). The sharp drop in potency between **17** and **19** can be understood by the structural changes in the binding mode with all three NOS species (Figure 7). In rnNOS, **19** shows a binding mode like **17** with its difluorobenzene bent-back toward the heme plane (Figure 7A). However, relative to the heme plane in the anchoring group, the 2-aminopyridine in **17** or the 2-aminopyrimidine in **19** shows a different dihedral angle, with the ethyl linker leading to the difluorobenzene ring in each inhibitor adopting a quite different twist to bring the difluorobenzene to the similar bent-back position close to Met570 in rnNOS. Although the H-bonds with Glu592 are maintained in both **17** and **19**, the 2-aminopyridine ring of **17** and the carboxylate group of Glu592 are almost co-planar (Figure 3B), while the 2-aminopyrimidine ring of **19** is at an angle relative to the carboxylate plane of Glu592 (Figure 7A). The co-planar H-bonds in **17** better optimize the H-bonding strength, potentially explaining the superior potency of **17**.

The underlying reason for the observed difference in the H-bonding geometry is the differences in basicity between the 2-aminopyridine and 2-aminopyrimidine, which was thus effectively explored by this design.

The binding mode variations between **17** and **19** were observed in hnNOS as well. The geometrical alignment between 2-aminopyridine of **17** and Glu597 (Figure 4B) is again more favorable than that between the 2-aminopyrimidine of **19** and Glu597 (Figure 7B). The difluorobenzene ring curls upward into a pocket and H-bonds with Tyr593. This is a rarely seen orientation for nNOS inhibitors, different from the more commonly observed upward position seen for **17**, where it H-bonds with Tyr567 instead (Figure 4B). The two aromatic rings of **19** in this binding mode are twisted closely against each other, which likely results in high internal energy strain.

Compound **19** binds to heNOS (Figure 7C) in a mode like that seen in the heNOS-**18** structure (Figure 6C). Again, the difluorobenzene covers both propionates, which enables the amine tail to be positioned out toward propionate A. Overall, the conformation of **19** in heNOS looks more relaxed compared to the more strained conformation seen in hnNOS (Figure 7B).

Effects of enhancing the lipophilicity of nNOS inhibitors by tail amine modification (20-22)—The potencies of **20**-**22**, which contain variations at the tail amine, toward rnNOS and hnNOS are comparable (Table 1). Compound **20** is the simplest among the three, having a secondary amine tail. **20** binds to rnNOS in an unusual upward mode (Figure 8A), but it is identical to the upward mode in hnNOS-**20** (Figure 8B). As noted

above, the upward mode in rnNOS-**18** (Figure 6A) had some subtle differences from the "normal" upward mode seen in hnNOS. In both the rnNOS-**20** and hnNOS-**20** case, the tail amine can reach the water molecule in between the H_4B and propionate A to make an H-bond (Figures 8A and 8B).

When the tail amino group is a tertiary diethylamine as in **21**, it turns to the normally observed bent-back mode in binding to rnNOS (Figure 9A) but is still in an upward binding mode in hnNOS (Figure 9B). The bulky tertiary amine of **21** cannot reach the water molecule between H_4B and propionate A for an H-bond in rnNOS (Figure 9A). However, in hnNOS the tertiary amine of **21** does form an H-bond with the water molecule (Figure 9B). Another unusual feature in the binding mode of **21** in hnNOS is that the difluorobenzene position, aided with a different twist of the ethylene linker, has moved slightly away from Tyr567. The H-bond between the F atom of **21** and Tyr567 becomes weaker. The reason for this new twist is not totally clear, but the nonbonded contacts between the tail diethylamine of **21** and Met341 and Trp683 might play a role (Figure 9B).

Compound **20** binds to heNOS in a unique way while the difluorobenzene covers the top of both propionates. The tail amino group protrudes directly in between H_4B and propionate A, where the water molecule normally sits (Figure 8C). Surprisingly, the ability to H-bond with both H_4B and heme did not translate to a tighter binding affinity of heNOS for **20** (Table 1). A bent-back binding mode was observed for **21** in heNOS (Figure 9C), which is unusual for NOS inhibitor binding to heNOS but is the normal mode for binding to rnNOS. The tail diethylamino group of **21** is attracted to Phe105 in heNOS by hydrophobic interactions rather than approaching the pterin water site. The bulky Phe105 in heNOS apparently imposes a higher influence on the tail amine position than Leu337 in rnNOS.

The third compound in this section, **22**, has a piperazine ring as the tail group. The electron density in the rnNOS-**22** complex was ambiguous. It was difficult to judge whether **22** bound in a bent-back or an upward mode. Nevertheless, in the hnNOS-**22** structure, **22** was observed in its regular upward conformation (Figure 10A), as expected. While one of the F atoms from the difluorobenzene H-bonds with Tyr567, the tail piperazine cannot orient its two ring N atoms to form a H-bond with the pterin site water molecule (Figure 10A). In heNOS, **22** was observed in a bent-back conformation (Figure 10B) like that seen with heNOS-**21** (Figure 9C). The piperazine ring can reach out to Phe105 for nonbonded contacts (Figure 10B). These types of nonpolar contacts might be a key factor in promoting the bent-back mode in both heNOS-**21** and heNOS-**22**, making it one of the possible inhibitor binding modes. In contrast, the piperazine in hnNOS-**22** contacts Met341 (Figure 10A) because the His342 in hnNOS, equivalent to Phe106 in heNOS, is too short to approach the tail piperazine of **22**.

Effects of changing the basicity of 2-aminopyridine of nNOS inhibitors (23, 24)—Compounds **23** and **24** were designed to have an altered basicity of the 2-aminopyridine by introducing fluorine atoms at the 4-position of the pyridine ring. In the rnNOS-**23** structure, **23** was found in the normal bent-back conformation (Figure 11A). The difluorobenzene is well accommodated in the active site. The difluoromethyl group of the 2-aminopyridine has one of its F-atoms H-bonding with the backbone amide N atom of

Gly586. The tail tertiary amine approaches the pterin site water but is too far for an H-bond. The binding of **23** to hnNOS is a bit unclear as indicated by the poor density around the difluorobenzene in the upward mode (Figure 11B). One of the F atoms of difluoromethyl group accepts an H-bond from the amide N atom of Gly591, and the tail amino group reaches to the pterin site water. Even though the binding mode of **23** appears to be normal in both structures of rnNOS and hnNOS, the potency of **23** is 22-fold- and 14-fold lower, respectively, toward the two nNOSs than **17**. The reason for the poor potency of **23** may not be mainly structural in nature, even though the bulky difluoromethyl group does disturb the normal positions of both 2-aminopyridine and difluorobenzene rings (as compared to when the 4-position is merely a methyl group as in **17**) as indicated by the choppy density observed in the hnNOS-**23** structures (Figure 11B). More likely, the lower basicity of the 2-aminopyridine of **23** weakens the H-bonding strength with Glu592 compared to **17** (Table 1).

The binding mode of **23** observed in heNOS (Figure 11C) is almost identical to that seen for many others in the series. That is, the ethylene linker from the 2-aminopyridine brings the difluorobenzene upward covering both propionates and with the tail amine displacing the pterin site water molecule, even though an H-bond may or may not form between the amine and propionate A. The same binding pattern was observed for **18, 19, 20**, and **23** bound to heNOS, displayed in Figures 6C, 7C, 8C, and 11C, respectively. In contrast, the other conformation, the bent-back mode seen in heNOS-**21** and heNOS-**22** (Figure 9C and 10B, respectively), is seen when the inhibitor has a long nonpolar moiety in the tail amine that can reach Phe105. Unfortunately, protein inhibitor interactions alone cannot fully explain the poor potency of the new NOS inhibitors for heNOS as reported in Table 1. Other factors, such as non-active site regions of the heNOS enzyme, including the dimer interface involving cofactor H_4B binding and the electron transfer reactions from the reductase to the oxygenase domain, all play important roles in the enzymatic activity of heNOS that could be modulated by inhibitor binding.

The bulky 4-trifluoromethyl group in **24** posed a serious challenge to obtaining structural data for **24**. So far, no good quality inhibitor density was observed with either the hnNOS-**24** data at 2.05 Å resolution or the heNOS-**24** data at 2.20 Å (unpublished observation). In both cases, the data provided good electron density for the protein structures but the interpretable density for **24** was limited to the 4-trifluoromethyl-2-aminopyridine moiety (see Figure S2 for details). The much poorer potencies of **24** across all NOS species in this study indicate that the poor potency of **24** is due not only to the poor H-bonding strength from the 4-trifluoromethyl-2-aminopyridine to the active site Glu residue, as seen for **23**, but also the bulkiness of the 4-trifluoromethyl group resulting in steric clashes that prevent an optimal fit of the tail portion of **24** into the active site.

Conclusions

We have developed a series of potent, selective, and highly permeable hnNOS inhibitors based on a 2,3-difluorobenzene linked 2-aminopyridine scaffold with different functionalities at the 4-position as well as alterations at the amino tail group. We identified a novel nNOS inhibitor, **17**, in this series, that showed excellent potency for rat (K_i = 15

nM) and human nNOS (K_i = 19 nM), with a selectivity of 1075-fold over human eNOS and 115-fold over human iNOS. In addition, **17** displayed excellent cell-membrane permeability (P_e = 13.7 x 10^{-6} cm s^{-1}) along with significantly low P-gp and BCRP substrate liability as indicated by its low efflux ratio (ER = 0.48) in the Caco-2 bidirectional assay. Finally, it has good metabolic stability in both mouse (MLM) and human liver microsomes (HLM), with a half-life of 29 min and > 60 min, respectively. Our results suggest that a slight change in substitution at the 4-position of the 2-aminopyridine scaffold considerably alters K_i values and other properties of the inhibitors with the three NOS isoforms. Generally, we found that increasing lipophilicity by incorporating fluorine atoms at the 4-position of the inhibitors (**23** and **24**) significantly increased blood-brain barrier permeability, as expected; however, it had a negative impact on potency. Increasing rigidity in the molecule (**10**-**14**) also had a positive impact on permeability, although both exhibited decreased potency and isoform selectivity. Finally, our detailed enzyme-inhibitor X-ray crystal structures of representative inhibitors, including **17**, bound to three NOS isoforms, provide a structural basis for the observed inhibitor potency and isoform selectivity. Overall, this study provides an important framework for the continued development of nNOS inhibitors for use in the treatment of neurodegenerative disease.

Experimental Section

Chemistry.

General procedures.—Unless otherwise stated, all described reactions were performed under an argon atmosphere. All reagents, including anhydrous solvents such as THF, 1,4-dioxane, CH_2Cl_2, MeOH, Et_3N, and DMF, were purchased from Sigma-Aldrich, Combi-blocks, Oakwood, and Astatech chemical companies. Metal catalysts tetrakis(triphenylphosphine)palladium(0), bis(triphenylphosphine)palladium(II) dichloride, copper(I) iodide, and Pd/C (10 wt. % loading (dry basis), matrix carbon powder, wet support) were purchased from either Strem Chemicals or Sigma-Aldrich. Sonogashira cross-coupling reactions were performed using Chemglass pressure vessels. All reactions were monitored by thin-layer chromatography (TLC) using Merck TLC silica gel 60 F_{254}; 0.25 mm glass plates and components were visualized by ultraviolet light (254 nm) and/or $KMnO_4$ or phosphomolybdic acid stain. Flash column chromatography was performed on an Agilent 971-FP automated flash purification system with a Varian column station and various SiliCycle cartridges (4–80 g, 40–63 μm, 60 Å). The general synthetic procedures for all compounds are discussed in Supporting Information. ^1H and ^{13}C NMR spectra were recorded on a Bruker Avance III NMR spectrometer with an operating frequency of 500 and 126 MHz, respectively, in $CDCl_3$, CD_3OD, or DMSO. Chemical shifts are reported in parts per million, and multiplicities are indicated by s = singlet, d = doublet, t = triplet, q = quartet, sep = septet, dd = doublet of doublet, dt = doublet of triplet, m = multiplet, and br = broad resonance. Coupling constants “J” were reported in hertz. High-resolution mass spectral (HRMS) data were obtained on an Agilent 6210 LC-TOF spectrometer in the positive ion mode using electrospray ionization (ESI) with an Agilent G1312A high-performance liquid chromatography (HPLC) pump and an Agilent G1367B autoinjector at the Integrated Molecular Structure Education and Research Center (IMSERC), Northwestern University. All final products used in assays were >95% pure.

General procedure for Sonogashira cross-coupling reaction (compounds 10-12, 39-41, 44, 49, 51, 53, 57, 60, 62, 66, and 68)

Compounds **10-12, 39-41, 44, 49, 51, 53, 57, 60, 62, 66**, and **68** were prepared following a reported procedure with slight modifications.[40,60] A flame-dried pressure vessel containing the bromo compounds (**29-31, 35-36, 42-43, 48, 56, 59, 65;** 1.0 equiv), $Pd(PPh_3)_4$ or $PdCl_2(dppf)$ or $PdCl_2(PPh_3)_2$ (5 mol %), and CuI (10 mol%), was filled with argon using three vacuum-argon flush cycles to remove oxygen. To this mixture, CH_3CN (0.12 - 0.23 M), Et_3N (4.0 equiv), and alkyne (**38, 45, 50, 54, 61**, and **67;** 1.2 equiv), were added, and the resulting mixture, was stirred for 12-24 h at 120 °C. After completion of the reaction as indicated by TLC, the reaction mixture was cooled to 25 °C, filtered through Celite, and concentrated by a rotary evaporation. Purification of the crude residue was performed by flash column chromatography eluting with hexane:EtOAc (20:80, v:v) for 10 min to remove any nonpolar residue, then followed by the solvent mixture DCM:CH_3OH:Et_3N, 80:10:10, v:v for another 15 min to afford **10-12, 39-41, 44, 49, 51, 53, 57, 60, 62, 66**, and **68.**

General procedure for reduction of the alkyne to the olefin (compounds 13 and 14)

Compounds **13** and **14** were prepared following a reported procedure with slight modifications.[56] A flame-dried round-bottom flask containing the alkyne (**10** or **11;** 1.0 equiv) was filled with THF and $LiAlH_4$ (1 equiv) was added portionwise over about 5 min at 25 °C under an argon atmosphere. The resulting heterogeneous mixture was heated at 40 °C with stirring for 5 h. After completion of the reaction, the reaction mixture was cooled to 0 °C and quenched with NH_4Cl dropwise. The organic phase was separated, and the aqueous phase was extracted thrice with DCM. The combined organic layers were washed with brine, dried over Na_2SO_4, filtered, and concentrated under reduced pressure. The crude product was purified by reverse phase flash column chromatography eluting with CH_3CN:H_2O (10:90, v:v) to CH_3CN:H_2O (30:70, v:v) to afford **13** or **14**.

General procedure for hydrogenation (compounds 15-24)

Compounds **15-24** were prepared following a reported procedure with slight modifications.[40] A flame-dried round-bottom flask containing the alkyne (**10-12, 39-41, 51, 57, 62**, and **69;** 1.0 equiv) was filled with CH_3OH and degassed for 15 min under a nitrogen atmosphere before adding a catalytic amount of Pd/C (10-40% of the weight of the substrate). The inert atmosphere of this heterogeneous mixture was replaced with a hydrogen balloon, and stirring was continued for 24 h at 25 °C. The crude mixture was then filtered through a pad of Celite, and the filtrate, was concentrated under reduced pressure. The crude product was purified by flash column chromatography eluting with hexane:EtOAc (20:80, v:v) for 10 min to remove any nonpolar residue then followed by the solvent mixture DCM:CH_3OH:Et_3N, 80:10:10, v:v for another 15 min to afford **15-24**.

General procedure for conversion to the HCl salt (10-24)

The freebase of compounds **10-24** were converted to their dihydrochloride salts by treatment with excess hydrogen chloride solution (3.0 M in CH_3OH) at 0 °C under an argon atmosphere. The resulting mixture was slowly warmed to 25 °C and stirring continued

for 8 h before evaporation of the solvent under reduced pressure using a rotary evaporator to afford the dihydrochloride salt of compounds **10-24.**

6-((5-((Dimethylamino)methyl)-2,3-difluorophenyl)ethynyl)-4-methylpyridin-2-amine (10)

Compound **10** was prepared by following the general procedure for the Sonogashira cross-coupling reaction starting from bromo compound **42** (473 mg, 1.89 mmol), alkyne **38** (300 g, 2.27 mmol), $Pd(PPh_3)_4$ (109 mg, 0.95 mmol), CuI (36 mg, 0.19 mmol), Et_3N (1.05 mL, 7.56 mmol). Compound **10** was isolated as a yellow solid (78 mg, 0.259 mmol, 82%). **^{1}H NMR** (500 MHz, CD_3OD): δ 7.31 – 7.27 (m, 2 H), 6.74 (s, 1 H), 6.43 (s, 1 H), 3.43 (s, 2 H), 2.23 (s, 6 H), 2.22 (s, 3 H). **^{13}C NMR** (126 MHz, CD_3OD): δ 159.7, 150.1 (dd, $J_{C\text{-}F}$ = 243.2, 11.3 Hz), 149.5 (2xC), 149.8 (dd, $J_{C\text{-}F}$ = 247.0, 13.9 Hz), 138.8, 135.3, 128.9, 118.6 (d, $J_{C\text{-}F}$ = 17.6 Hz), 118.3, 109.7, 94.3, 79.0, 62.0, 43.8, 19.4. **HRMS** (ESI) Calcd for $C_{17}H_{18}F_2N_3$ $[(M+H)^+]$: 302.1463, found: 302.1472.

6-((5-(2-(Dimethylamino)ethyl)-2,3-difluorophenyl)ethynyl)-4-methylpyridin-2-amine (11)

Compound **11** was prepared by following the general procedure for the Sonogashira cross-coupling reaction starting from bromo compound **30** (833 mg, 3.15 mmol), alkyne **38** (500 mg, 3.78 mmol), $PdCl_2$dppf (129 mg, 0.16 mmol), Et_3N (1.76 mL, 12.6 mmol), and CuI (60.0 mg, 0.315 mmol). Compound **11** was isolated as a deep brown solid (1.01 g, 3.22 mmol, 82%). **^{1}H NMR** (500 MHz, CD_3OD): δ 7.26 – 7.16 (m, 2 H), 6.73 (s, 1 H), 6.43 (s, 1 H), 2.77 (dd, J = 9.5, 6.4 Hz, 2 H), 2.56 (dd, J = 9.5, 6.4 Hz, 2 H), 2.29 (s, 6 H), 2.22 (s, 3 H). **^{13}C NMR** (126 MHz, CD_3OD): δ 161.1, 151.5 (dd, $J_{C\text{-}F}$ = 247.0 12.6 Hz), 150.9, 150.5 (dd, $J_{C\text{-}F}$ = 252.0, 13.9 Hz), 140.3, 138.6 (dd, $J_{C\text{-}F}$ = 6.3, 5.0 Hz), 129.6 (d, $J_{C\text{-}F}$ = 3.8 Hz), 119.5 (d, $J_{C\text{-}F}$ = 17.6 Hz), 114.0 (d, $J_{C\text{-}F}$ = 12.6 Hz), 111.1, 95.5 (d, $J_{C\text{-}F}$ = 3.8 Hz), 80.6 (d, $J_{C\text{-}F}$ = 5.0 Hz), 61.5, 45.3, 33.5, 20.8. **HRMS** (ESI) Calcd for $C_{18}H_{20}F_2N_3$ $[(M+H)^+]$: 316.1620, found: 316.1623.

4-chloro-6-((5-(2-(Dimethylamino)ethyl)-2,3-difluorophenyl)ethynyl)pyridin-2-amine (12)

Compound **12** was prepared by following the general procedure for the Sonogashira cross-coupling reaction starting from bromo compound **30** (656 mg, 2.48 mmol), alkyne **45** (455 mg, 2.98 mmol), $Pd(PPh_3)_4$ (86 mg, 0.075 mmol), Et_3N (1.39 mL, 9.94 mmol), and CuI (47.3 mg, 0.248 mmol). Compound **12** was isolated as a deep brown solid (142 mg, 0.423 mmol, 65%). **^{1}H NMR** (500 MHz, CD_3OD): δ 7.32 – 7.23 (m, 2 H), 6.87 (d, J = 1.7 Hz, 1 H), 6.63 (d, J = 1.7 Hz, 1 H), 2.82 (dd, J = 9.3, 6.6 Hz, 2 H), 2.67 (dd, J = 9.4, 6.4 Hz, 2 H), 2.37 (s, 6 H). **^{13}C NMR** (126 MHz, CD_3OD): δ 161.9, 151.5 (dd, $J_{C\text{-}F}$ = 248.2, 12.6 Hz), 150.7 (dd, $J_{C\text{-}F}$ = 252.0, 13.9 Hz), 146.0, 142.2, 138.4 (dd, $J_{C\text{-}F}$ = 6.3, 5.0 Hz), 129.8 (d, $J_{C\text{-}F}$ = 3.8 Hz), 120.0 (d, $J_{C\text{-}F}$ = 17.6 Hz), 117.6, 113.6 (dd, $J_{C\text{-}F}$ = 11.3, 1.3 Hz), 109.9, 94.4 (d, $J_{C\text{-}F}$ = 3.8 Hz), 81.7 (d, $J_{C\text{-}F}$ = 3.8 Hz), 61.3, 45.2, 33.2. **HRMS** (ESI) Calcd for $C_{17}H_{17}ClF_2N_3$ $[(M+H)^+]$: 336.1074, found: 336.1085.

(*E*)-6-(5-((Dimethylamino)methyl)-2,3-difluorostyryl)-4-methylpyridin-2-amine (13)

Compound **13** was prepared by following the general procedure for the reduction of alkyne to olefin starting from alkyne **10** (40 mg, 0.133 mmol) and $LiAlH_4$ (15 mg, 0.40 mmol). Compound **13** was isolated as a deep yellow solid (10 mg, 0.033 mmol, 25%). **^{1}H NMR**

(500 MHz, CD_3OD): δ 7.56 (d, *J* = 16.2 Hz, 1 H), 7.44 (dt, *J* = 6.1, 1.8 Hz, 1 H), 7.19 – 7.11 (m, 2 H), 6.65 (d, *J* = 1.2 Hz, 1 H), 6.36 (t, *J* = 1.1 Hz, 1 H), 3.47 (s, 2 H), 2.27 (s, 6 H), 2.24 (s, 3 H). **^{13}C NMR** (126 MHz, CD_3OD): δ 161.0, 153.8, 151.9 (dd, $J_{C\text{-}F}$ = 247.0, 13.9 Hz), 150.9, 148.9 (dd, $J_{C\text{-}F}$ = 250.7, 12.6 Hz), 136.1 (t, $J_{C\text{-}F}$ = 5.0 Hz), 133.1 (d, $J_{C\text{-}F}$ = 5.0 Hz), 124.3, 123.3 (t, $J_{C\text{-}F}$ = 3.8 Hz), 117.9 (d, $J_{C\text{-}F}$ = 17.6 Hz), 115.5, 110.2, 63.9, 45.2, 20.9. **HRMS** (ESI) Calcd for $C_{17}H_{20}F_2N_3$ [$(M+H)^+$]: 304.1620, found: 304.1625.

(*E*)-6-(5-(2-(Dimethylamino)ethyl)-2,3-difluorostyryl)-4-methylpyridin-2-amine (14)

Compound **14** was prepared by following the general procedure for the reduction of alkyne to olefin starting from alkyne **11** (24 mg, 0.076 mmol), and $LiAlH_4$ (3.5 mg, 0.091 mmol). Compound **14** was isolated as a yellow solid (6 mg, 0.019 mmol, 25%). **^{1}H NMR** (500 MHz, CD_3OD): δ 7.53 (d, *J* = 16.2 Hz, 1 H), 7.38 – 7.29 (m, 1 H), 7.13 (d, *J* = 16.2 Hz, 1 H), 7.07 (ddd, *J* = 11.0, 7.3, 2.1 Hz, 1 H), 6.65 (s, 1 H), 6.36 (s, 1 H), 2.80 (dd, *J* = 9.8, 6.4 Hz, 2 H), 2.60 (dd, *J* = 9.9, 6.3 Hz, 2 H), 2.32 (s, 6 H), 2.24 (s, 3 H). **^{13}C NMR** (126 MHz, CD_3OD): δ 161.0, 153.9, 151.9 (dd, $J_{C\text{-}F}$ = 245.7, 12.6 Hz), 150.9, 148.3 (dd, $J_{C\text{-}F}$ = 249.5, 13.9 Hz), 138.1 (dd, $J_{C\text{-}F}$ = 6.3, 5.0 Hz), 132.9 (d, $J_{C\text{-}F}$ = 6.3 Hz), 128.1 (d, $J_{C\text{-}F}$ = 8.8 Hz), 123.6, 123.5, 117.4 (d, $J_{C\text{-}F}$ = 17.6 Hz), 115.4, 110.1, 61.8, 45.4, 33.9, 20.9. **HRMS** (ESI) Calcd for $C_{18}H_{22}F_2N_3$ [$(M+H)^+$]: 318.1776, found: 318.1780.

6-(5-((Dimethylamino)methyl)-2,3-difluorophenethyl)-4-methylpyridin-2-amine (15)

Compound **15** was prepared by following the general procedure for the hydrogenation reaction starting from **41** (232 g, 0.627 mmol), Pd/C (60 mg, 25 % of the weight of the substrate), and a hydrogen balloon. Compound **15** was isolated as a pale-yellow solid (190 mg, 0.501 mmol, 81%). **^{1}H NMR** (500 MHz, CD_3OD): δ 7.44 – 7.42 (m, 2 H), 6.66 (s, 1 H), 6.61 (s, 1 H), 4.31 (s, 2 H), 3.17 (dd, *J* = 8.8, 6.5 Hz, 2 H), 3.08 (dd, *J* = 8.7, 6.5 Hz, 2 H), 2.85 (s, 6 H), 2.33 (s, 3 H). **^{13}C NMR** (126 MHz, CD_3OD): δ 158.7, 156.1, 151.6 (dd, $J_{C\text{-}F}$ = 249.5, 13.9 Hz), 151.0 (dd, $J_{C\text{-}F}$ = 250.7, 13.9 Hz), 149.5, 131.4 (d, $J_{C\text{-}F}$ = 12.6 Hz), 130.0 (t, $J_{C\text{-}F}$ = 3.8 Hz), 128.1 (dd, $J_{C\text{-}F}$ = 6.3, 5.0 Hz), 119.6 (d, $J_{C\text{-}F}$ = 18.9 Hz), 115.0, 111.0, 60.8, 43.0, 33.9, 28.7, 21.9. **HRMS** (ESI) Calcd for $C_{17}H_{22}F_2N_3$ [$(M+H)^+$]: 306.1776, found: 306.1790.

6-(5-(2-(Dimethylamino)ethyl)-2,3-difluorophenethyl)pyridin-2-amine dihydrochloride (16).

Compound **16** was prepared by following the general procedure for the hydrogenation reaction starting from **12** (259 mg, 0.77 mmol), Pd/C (78 mg, 30% of the weight of the substrate) and a hydrogen balloon. Compound **16** was isolated as a white solid (188 mg, 0.616 mmol, 80%). **^{1}H NMR** (500 MHz, CD_3OD): δ 7.82 (dd, *J* = 8.9, 7.1 Hz, 1H), 7.18 (t, *J* = 8.2 Hz, 2H), 6.89 (d, *J* = 8.9 Hz, 1H), 6.69 (d, *J* = 7.1 Hz, 1H), 3.44 – 3.36 (m, 2H), 3.18 – 3.02 (m, 6H), 2.96 (s, 6H). **^{13}C NMR** (126 MHz, CD_3OD): δ 156.3, 151.6 (dd, $J_{C\text{-}F}$ = 247.6, 13.4 Hz), 150.1, 149.2 (dd, $J_{C\text{-}F}$ = 245.6, 13.0 Hz), 145.7, 134.5 (dd, $J_{C\text{-}F}$ = 6.2, 4.5 Hz), 130.4 (d, $J_{C\text{-}F}$ = 12.7 Hz), 127.4 (d, $J_{C\text{-}F}$ = 3.3 Hz), 117.3 (d, $J_{C\text{-}F}$ = 17.9 Hz), 113.1, 112.2, 59.3, 43.7, 34.1, 30.9, 28.8. **HRMS** (ESI) Calcd for $C_{17}H_{22}F_2N_3$ [$(M+H)^+$]: 306.1776, found: 306.1783.

6-(5-(2-(dimethylamino)ethyl)-2,3-difluorophenethyl)-4-methylpyridin-2-amine dihydrochloride (17)

Compound **17** was prepared by following the general procedure for the hydrogenation reaction starting from **11** (0.70 g, 2.22 mmol), Pd/C (140 mg, 20% of the weight of the substrate), and a hydrogen balloon. Compound **17** was isolated as a brown oil (0.57 g, 1.78 mmol, 80%). **^{1}H NMR** (500 MHz, $CDCl_3$): δ 6.94 (ddd, J = 11.2, 7.3, 2.2 Hz, 1H), 6.77 (dt, J = 6.0, 1.8 Hz, 1H), 6.25 (s, 1H), 6.23 (s, 1H), 2.99 – 2.95 (m, 2 H), 2.80 – 2.77 (m, 2 H), 2.71 – 2.67 (m, 2 H), 2.50 – 2.46 (m, 2 H), 2.29 (s, 6H), 2.14 (s, 3H). **^{13}C NMR** (126 MHz, $CDCl_3$): δ 160.7, 159.0, 151.5 (dd, J = 245.7, 13.9 Hz), 151.0, 148.6 (dd, J = 244.4, 12.6 Hz), 137.4 (dd, J = 6.3, 3.8 Hz), 131.8 (d, J = 13.9 Hz), 126.9 (t, J = 3.8 Hz), 116.0 (d, J = 17.6 Hz), 114.6, 108.1, 61.9, 45.3, 38.7, 33.7, 30.0 (t, J = 1.9 Hz), 21.0. **HRMS** (ESI) Calcd for $C_{18}H_{24}F_2N_3$ $[(M+H)^+]$: 320.1933, found: 320.1943.

6-(5-(2-(Dimethylamino)ethyl)-2,3-difluorophenethyl)-4-methoxypyridin-2-amine dihydrochloride (18).

Compound **18** was prepared by following the reported procedure with a slight modification.[57] A solution of **52** (0.13 g, 0.30 mmol) in 95% H_2SO_4 (10 mL) was stirred at 80 °C for 1 h under an argon atmosphere. The dark solution was poured into ice and neutralized to pH 14 using NaOH pellets. The organic fraction was separated from the aqueous phase. The aqueous phase was further extracted with DCM (3 x 50 mL). The combined organic layers were washed with brine, dried over Na_2SO_4, filtered, and concentrated under reduced pressure. The crude product was further purified by flash column chromatography, eluting with hexane:EtOAc (50:50, v:v) for 10 min to remove any nonpolar residue then followed by the solvent mixture DCM:CH_3OH:Et_3N, 70:20:10, v:v for another 15 min to afford **18** as a pale-yellow solid (62 mg, 0.185 mmol, 62%). **^{1}H NMR** (500 MHz, CD_3OD): δ 7.19 – 7.15 (m, 2 H), 6.33 (d, J = 2.1 Hz, 1 H), 6.26 (d, J = 1.6 Hz, 1 H), 3.92 (s, 3 H), 3.42 – 3.35 (m, 2 H), 3.12 – 2.99 (m, 6 H), 2.95 (s, 6 H). **^{13}C NMR** (126 MHz, CD_3OD): δ 172.6, 157.9, 151.6 (dd, $J_{C\text{-}F}$ = 247.7, 13.4 Hz), 151.3, 149.2 (dd, $J_{C\text{-}F}$ = 245.8, 13.0 Hz), 134.5 (dd, $J_{C\text{-}F}$ = 6.1, 4.4 Hz), 130.4 (d, $J_{C\text{-}F}$ = 12.6 Hz), 127.4, 117.3 (d, $J_{C\text{-}F}$ = 17.8 Hz), 105.1, 91.6, 59.4, 57.4, 43.7, 34.0, 30.9, 28.7. **HRMS** (ESI) Calcd for $C_{18}H_{24}F_2N_3O$ $[(M+H)^+]$: 336.1882, found: 336.1882.

4-(5-(2-(Dimethylamino)ethyl)-2,3-difluorophenethyl)-6-methylpyrimidin-2-amine dihydrochloride (19).

Compound **19** was prepared by following the general procedure for the hydrogenation reaction starting from **57** (76 mg, 0.24 mmol), Pd/C (23 mg, 30% of the weight of the substrate), and a hydrogen balloon. Compound **19** was isolated as a yellow-viscous oil (63 mg, 0.197 mmol, 82%). **^{1}H NMR** (500 MHz, CD_3OD): δ 7.16 (ddt, J = 12.5, 5.4, 2.3 Hz, 2H), 6.84 (s, 1H), 3.42 – 3.34 (m, 2H), 3.18 – 3.11 (m, 2H), 3.11 – 3.01 (m, 4H), 2.95 (s, 6H), 2.49 (s, 3H). **^{13}C NMR** (126 MHz, CD_3OD): δ 157.5 (2xC), 151.7 (dd, $J_{C\text{-}F}$ = 247.5, 13.3 Hz), 149.2 (dd, $J_{C\text{-}F}$ = 245.7, 12.8 Hz), 134.4 (d, $J_{C\text{-}F}$ = 4.3 Hz), 134.3 (d, $J_{C\text{-}F}$ = 4.6 Hz), 131.1 (d, $J_{C\text{-}F}$ = 12.7 Hz), 127.3 (t, $J_{C\text{-}F}$ = 3.2 Hz), 117.1 (d, $J_{C\text{-}F}$ = 17.9 Hz), 111.0, 59.3, 43.6, 37.5, 30.9, 27.5, 20.9. **HRMS** (ESI) Calcd for $C_{17}H_{23}F_2N_4$ $[(M+H)^+]$: 321.1885, found: 321.1891.

6-(5-(2-Aminoethyl)-2,3-difluorophenethyl)-4-methylpyridin-2-amine dihydrochloride (20)

Compound **20** was prepared by following the general procedure for the hydrogenation reaction starting from **39** (210 mg, 0.73 mmol), Pd/C (63 mg, 30% of the weight of the substrate), and a hydrogen balloon. Compound **20** was isolated as an off-white solid (150 mg, 0.52 mmol, 70%). **^{1}H NMR** (500 MHz, CD_3OD): δ 7.16 – 7.11 (m, 2 H), 6.71 (s, 1 H), 6.60 (s, 1 H), 3.21 – 3.15 (m, 2 H), 3.14 – 3.10 (m, 2 H), 3.06 – 3.02 (m, 2 H), 2.98 – 2.94 (m, 2 H), 2.34 (s, 3 H).**^{13}C NMR** (126 MHz, CD_3OD): δ 159.0, 155.8, 151.6 (dd, *J* = 247.0, 12.6 Hz), 149.2, 149.1 (dd, *J* = 245.7, 12.6 Hz), 135.1 (dd, *J* = 6.3, 3.8 Hz), 130.5 (d, *J* = 12.6 Hz), 127.3 (t, *J* = 3.2 Hz), 117.2 (d, *J* = 17.6 Hz), 115.0, 111.1, 41.6, 34.0, 33.6, 28.9, 21.9. **HRMS** (ESI) Calcd for $C_{16}H_{20}F_2N_3$ [$(M+H)^+$]: 292.1620, found: 292.1623.

6-(5-(2-(Diethylamino)ethyl)-2,3-difluorophenethyl)-4-methylpyridin-2-amine dihydrochloride (21)

Compound **21** was prepared by following the general procedure for the hydrogenation reaction starting from **40** (161 mg, 0.47 mmol), Pd/C (48 mg, 30% of the weight of the substrate), and a hydrogen balloon. Compound **21** was isolated as a pale-yellow solid (134 mg, 0.39 mmol, 82%). **^{1}H NMR** (500 MHz, $CDCl_3$): 6.82 (ddd, *J* = 10.9, 7.2, 2.2 Hz, 1 H), 6.72 (dt, *J* = 6.0, 1.8 Hz, 1 H), 6.30 (s, 1 H), 6.16 (s, 1 H), 4.38 (bs, 2 H), 3.01 – 2.97 (m, 2 H), 2.87 – 2.76 (m, 2 H), 2.66 – 2.53 (m, 8 H), 2.17 (s, 3 H), 1.04 (t, *J* = 7.2 Hz, 6 H). **^{13}C NMR** (126 MHz, $CDCl_3$): δ 159.0, 158.4, 150.3 (dd, *J* = 248.2, 13.9 Hz), 149.3, 147.4 (dd, *J* = 244.4, 12.6 Hz), 136.7 (dd, *J* = 6.3, 5.0 Hz), 130.8 (d, *J* = 13.9 Hz), 125.5 (t, *J* = 3.8 Hz), 115.0 (d, *J* = 17.6 Hz), 114.6, 106.7, 54.7, 47.0, 38.3, 32.9, 29.2, 21.0, 11.9. **hRMS** (ESI) Calcd for $C_{20}H_{28}F_2N_3$ [$(M+H)^+$]: 348.2246, found: 348.2249.

6-(2,3-Difluoro-5-(2-(4-methylpiperazin-1-yl)ethyl)phenethyl)-4-methylpyridin-2-amine dihydrochloride (22).

Compound **22** was prepared by following the general procedure for the hydrogenation reaction starting from **41** (232 mg, 0.63 mmol), Pd/C (70 mg, 30% of the weight of the substrate), and a hydrogen balloon. Compound **22** was isolated as a yellow solid (190 mg, 0.51 mmol, 81%). **^{1}H NMR** (500 MHz, CD_3OD): δ 6.93 (ddd, *J* = 11.3, 7.3, 2.2 Hz, 1 H), 6.75 (dt, *J* = 6.0, 1.8 Hz, 1 H), 6.24 (s, 1 H), 6.22 (s, 1 H), 2.99 – 2.94 (m, 2 H), 2.80 – 2.76 (m, 2 H), 2.71 – 2.67 (m, 2 H), 2.67 – 2.30 (m, 10 H), 2.29 (s, 3 H), 2.14 (s, 3 H). ^{13}C NMR (126 MHz, CD_3OD): δ 160.8, 159.0, 151.4 (dd, *J* = 245.7, 13.9 Hz), 151.0, 148.5 (dd, *J* = 243.2, 12.6 Hz), 137.7 (dd, *J* = 6.3, 3.8 Hz), 131.7 (d, *J* = 12.6 Hz), 126.9 (t, *J* = 3.8 Hz), 116.0 (d, *J* = 16.4 Hz), 114.7, 108.1, 61.0, 55.6, 53.6, 46.0, 38.7, 33.2, 30.0, 21.0. **HRMS** (ESI) Calcd for $C_{21}H_{29}F_2N_4$ [$(M+H)^+$]: 375.2355, found: 375.2358.

4-(Difluoromethyl)-6-(5-(2-(dimethylamino)ethyl)-2,3-difluorophenethyl)pyridin-2-amine dihydrochloride (23)

Compound **23** was prepared by following the reported procedure with a slight modification.[59] To a DCM (2 mL) solution of **63** (63 mg, 0.133 mmol) was added concentrated trifluoroacetic acid (2 mL) at room temperature, and the resulting mixture was heated to 80 °C for 8 h with stirring. After completion of the reaction, the mixture was concentrated under reduced pressure. The crude product was dissolved in EtOAc (10 mL)

and neutralized with aqueous NaOH (2 M) until pH ≥ 9. The organic phase was separated from aqueous phase. The aqueous phase was further extracted twice with EtOAc (2 x 50 mL). The combined organic layer was washed with brine (30 mL), dried over Na_2SO_4, filtered, and concentrated under reduced pressure using a rotary evaporator to afford **23** as a brown solid (40 mg, 0.113 mmol, 85%). **^{1}H NMR** (500 MHz, $CDCl_3$): δ 6.84 (ddd, *J* = 10.8, 7.2, 2.2 Hz, 1 H), 6.71 (dt, *J* = 6.0, 1.8 Hz, 1 H), 6.53 (s, 1 H), 6.45 (t, *J* = 56.0 Hz, 1 H), 6.44 (s, 1 H), 4.58 (s, 2 H), 3.04 – 3.01 (m, 2 H), 2.94 – 2.90 (m, 2 H), 2.69 – 2.66 (m, 2 H), 2.48 – 2.45 (m, 2 H), 2.28 (s, 6 H). **^{13}C NMR** (126 MHz, $CDCl_3$): δ 160.8, 158.6, 150.4 (dd, $J_{C\text{-}F}$ = 247.4, 13.3 Hz), 147.5 (dd, $J_{C\text{-}F}$ = 244.9, 12.7 Hz), 144.5 (t, $J_{C\text{-}F}$ = 22.8 Hz), 136.3 (t, $J_{C\text{-}F}$ = 5.0 Hz), 130.4 (d, $J_{C\text{-}F}$ = 12.7 Hz), 125.4 (t, $J_{C\text{-}F}$ = 3.2 Hz), 115.1 (d, $J_{C\text{-}F}$ = 17.1 Hz), 113.4 (t, $J_{C\text{-}F}$ = 240.9 Hz), 109.2 (t, $J_{C\text{-}F}$ = 5.6 Hz), 102.4 (t, $J_{C\text{-}F}$ = 6.5 Hz), 61.2, 45.5, 38.4, 33.6, 28.9 (t, $J_{C\text{-}F}$ = 2.3 Hz). **HRMS** (ESI) Calcd for $C_{18}H_{22}F_4N_3$ [$(M+H)^+$]: 356.1744, found: 356.1752.

6-(5-(2-(Dimethylamino)ethyl)-2,3-difluorophenethyl)-4-(trifluoromethyl)pyridin-2-amine (24)

Compound **24** was prepared by following the typical procedure for the hydrogenation reaction starting from **69** (84 mg, 0.23 mmol), Pd/C (25 mg, 30% of the weight of the substrate) and a hydrogen balloon. Compound **24** was isolated as an off-white solid (36 mg, 0.096 mmol, 42%). **^{1}H NMR** (500 MHz, $CDCl_3$): δ 6.96 (ddd, *J* = 11.2, 7.2, 2.1 Hz, 1 H), 6.79 (dt, *J* = 6.1, 1.8 Hz, 1 H), 6.61 (s, 1 H), 6.49 (s, 1 H), 3.12 – 2.96 (m, 2 H), 2.91 (dd, *J* = 8.5, 6.6 Hz, 2 H), 2.72 (dd, *J* = 10.2, 6.2 Hz, 2 H), 2.58 (dd, *J* = 10.2, 6.1 Hz, 2 H), 2.37 (s, 6 H). **^{13}C NMR** (126 MHz, $CDCl_3$): δ 161.9, 161.4, 151.5 (dd, *J* = 246.4, 13.3 Hz), 148.7 (dd, *J* = 243.9, 12.8 Hz), 141.3 (q, *J* = 32.8 Hz), 137.1 (dd, *J* = 243.9, 12.8 Hz 5.6, 4.8 Hz), 131.5 (d, *J* = 12.8 Hz), 126.9 (t, *J* = 3.2 Hz), 124.6 (q, *J* = 272.7 Hz), 116.2 (d, *J* = 17.4 Hz), 107.6 (q, *J* = 3.3 Hz), 103.2 (q, *J* = 4.1 Hz), 61.6, 45.1, 38.9, 33.4, 29.6 (t, *J* = 2.3 Hz). **HRMS** (ESI) Calcd for $C_{18}H_{21}F_5N_3$ [$(M+H)^+$]: 374.1650, found: 374.1662.

Supplementary Material

Refer to Web version on PubMed Central for supplementary material.

ACKNOWLEDGMENTS

We thank Radoslaw T. Chrzanowski for assistance in the MOE docking studies. This work made use of the IMSERC at Northwestern University, which has received support from the Soft and Hybrid Nanotechnology Experimental (SHyNE) Resource (NSF ECCS-2025633); the State of Illinois and International Institute for Nanotechnology (IIN). We also thank the beamline staff at SSRL and ALS for their assistance during the remote X-ray diffraction data collections.

FUNDING SOURCES

We are grateful for the generous support from the National Institutes of Health (R35GM131788 to R.B.S.; GM057353 and GM131920 to T.L.P.).

ABBREVIATIONS

BBB	blood–brain barrier
BCRP	breast-cancer-resistant protein

Caco-2	cancer coli-2
CaM	calmodulin
CNS	central nervous system
eNOS	endothelial nitric oxide synthase
ER	efflux ratio
FAD	flavin adenine dinucleotide
FMN	Flavin mononucleotide
H_4B	(6*R*)-5,6,7,8-tetrahydrobiopterin
heNOS	human endothelial nitric oxide synthase
hiNOS	human inducible nitric oxide synthase
iNOS	inducible nitric oxide synthase
hnNOS	human neuronal nitric oxide synthase
NADPH	reduced nicotinamide adenine dinucleotide phosphate
nNOS	neuronal nitric oxide synthase
NO	nitric oxide
P_{app}	apparent permeability
P_e	effective permeability
PAMPA	parallel artificial membrane permeability assay
P-gp	P-glycoprotein
rnNOS	rat neuronal nitric oxide synthase
TBAF	tetra-n-butylammonium fluoride
TFA	trifluoroacetic acid
TLC	thin layer chromatography

REFERENCES

(1). Vallance P, Leiper J Blocking NO synthesis: how, where and why? Nat. Rev. Drug Discovery 2002, 1, 939–950. [PubMed: 12461516]

(2). Kerwin JF Jr.; Lancaster JR; Feldman PL Nitric oxide: a new paradigm for second messengers. J. Med. Chem 1995, 38, 4343–4362. [PubMed: 7473563]

(3). Vincent SR Nitric oxide: a radical neurotransmitter in the central nervous system. Prog. Neurobiol 1994, 42, 129–160. [PubMed: 7480785]

(4). Ignarro LJ; Lippton H; Edwards JC; Baricos WH; Hyman AL; Kadowitz PJ; Gruetter CA Mechanism of vascular smooth muscle relaxation by organic nitrates, nitrites, nitroprusside

and nitric oxide: evidence for the involvement of S-nitrosothiols as active intermediates. J. Pharmacol. Exp. Ther 1981, 218, 739–749. [PubMed: 6115052]

(5). Palmer RM; Ferrige AG; Moncada S Nitric oxide release accounts for the biological activity of endothelium-derived relaxing factor. Nature 1987, 327, 524–526. [PubMed: 3495737]

(6). Bogdan C Nitric oxide and the immune response. Nat. Immunol 2001, 2, 907–916. [PubMed: 11577346]

(7). Alderton WK, Cooper CE, Knowles RG Nitric oxide synthases: structure, function and inhibition. Biochem. J 2001, 357, 593–615. [PubMed: 11463332]

(8). Esplugues JV NO as a signalling molecule in the nervous system. Br J Pharmacol. 2002, 135, 1079–1095. [PubMed: 11877313]

(9). Wang Y; Newton DC; Marsden PA Neuronal NOS: Gene Structure, mRNA Diversity, and Functional Relevance. Crit. Rev. Neurobiol 1999, 13, 21–43. [PubMed: 10223522]

(10). Barañano DE; Snyder SH Neural roles for heme oxygenase: contrasts to nitric oxide synthase. Proc. Natl. Acad. Sci. U.S.A 2001, 98, 10996–11002. [PubMed: 11572959]

(11). Karpuzoglu E; Ahmed SA Estrogen regulation of nitric oxide and inducible nitric oxide synthase (iNOS) in immune cells: implications for immunity, autoimmune diseases, and apoptosis. Nitric Oxide 2006, 15, 177–186. [PubMed: 16647869]

(12). Roe ND; Ren J Nitric oxide synthase uncoupling: a therapeutic target in cardiovascular diseases. Vasc. Pharmacol 2012, 57, 168–172.

(13). Knott AB; Bossy-Wetzel E Nitric Oxide in Health and Disease of the Nervous System, Antioxid. Redox Signal 2009, 11, 541–553. [PubMed: 18715148]

(14). Tewari D; Sah AN; Bawari S; Nabavi SF; Dehpour AR; Shirooie S; Braidy N; Fiebich BL; Vacca RA; Nabavi SM Role of Nitric Oxide in Neurodegeneration: Function, Regulation, and Inhibition, Curr. Neuropharmacol, 2021, 19, 114–126. 10.2174/1570159X18666200429001549 [PubMed: 32348225]

(15). Tripathi MK; Kartawy M; Amal H The role of nitric oxide in brain disorders: Autism spectrum disorder and other psychiatric, neurological, and neurodegenerative disorders, Redox Biology, 2020, 34, 101567. [PubMed: 32464501]

(16). Hall CN; Garthwaite J What is the real physiological NO concentration in vivo? Nitric Oxide. 2009, 21, 92–103. [PubMed: 19602444]

(17). Torreilles F; Salman-Tabcheh S; Guérin M; Torreilles J Neurodegenerative disorders: the role of peroxynitrite. Brain Res. Rev 1999, 30, 153–163. [PubMed: 10525172]

(18). Valko M; Leibfritz D; Moncol J; Cronin MTD; Mazur M; Telser J Free radicals and antioxidants in normal physiological functions and human disease, Int. J. Biochem. Cell Biol, 2007, 39, 44–84. [PubMed: 16978905]

(19). Cobb CA; Cole MP Oxidative and nitrative stress in neurodegeneration, Neurobiol. Dis, 2015, 84, 4–21. [PubMed: 26024962]

(20). Uehara T; Nakamura T; Yao D; Shi Z-Q; Gu Z; Ma Y; Masliah E; Nomura Y; Lipton SA S-Nitrosylated protein-disulphide isomerase links protein misfolding to neurodegeneration. Nature 2006, 441, 513–517. [PubMed: 16724068]

(21). Dorheim M-A; Tracey WR; Pollock JS; Grammas P Nitric oxide synthase activity is elevated in brain microvessels in Alzheimer′ s disease. Biochem. Biophys. Res. Commun 1994, 205, 659–665. [PubMed: 7528015]

(22). Zhang L; Dawson VL; Dawson TM Role of nitric oxide in Parkinson's disease. Pharmacol. Ther 2006, 109, 33–41. [PubMed: 16005074]

(23). Norris PJ; Waldvogel HJ; Faull RLM; Love DR; Emson PC Decreased neuronal nitric oxide synthase messenger RNA and somatostatin messenger RNA in the striatum of Huntington's disease. Neuronsicence 1996, 72, 1037–1047.

(24). Drechsel DA; Estévez AG; Barbeito L; Beckman JS Nitric oxide-mediated oxidative damage and the progressive demise of motor neurons in ALS. Neurotoxic. Res 2012, 22, 251–264.

(25). Ashina M Nitric oxide synthase inhibitors for the treatment of chronic tension-type headache. Exp. Opin. Pharmacother 2002, 3, 395–399.

(26). Sims NR; Anderson MF Mitochondrial contributions to tissue damage in stroke. Neurochem. Int 2002, 40, 511–526. [PubMed: 11850108]

(27). Mukherjee P; Cinelli MA; Kang S; Silverman RB Development of nitric oxide synthase inhibitors for neurodegeneration and neuropathic pain. Chem. Soc. Rev 2014, 43, 6814–6838. [PubMed: 24549364]

(28). Feng C Mechanism of Nitric Oxide Synthase regulation: electron transfer and interdomain interactions. Coord. Chem. Rev 2012, 256, 393–411. [PubMed: 22523434]

(29). Silverman RB Design of selective neuronal nitric oxide synthase inhibitors for the prevention and treatment of neurodegenerative diseases. Acc. Chem. Res 2009, 42, 439–451. [PubMed: 19154146]

(30). Kobayashi Y; Ikeda K; Shinozuka K; Nara Y; Yamori Y; Hattori K L-nitroarginine increases blood pressure in the rat. Clin. Exp. Pharmacol. Physiol 1991, 18, 397–399. [PubMed: 1914242]

(31). Cinelli MA; Do HT; Miley GP; Silverman RB Inducible nitric oxide synthase: Regulation, structure, and inhibition, Med. Res. Rev 2020, 40, 158–189. [PubMed: 31192483]

(32). Li H; Evenson RJ; Chreifi G; Silverman RB; Poulos TL Structural Basis for Isoform Selective Nitric Oxide Synthase Inhibition by Thiophene-2-carboximidamides, Biochemistry, 2018, 57, 6319–6325. [PubMed: 30335983]

(33). Poulos TL; Li H Structural basis for isoform-selective inhibition in nitric oxide synthase. Acc. Chem. Res 2013, 46, 390–398. [PubMed: 23030042]

(34). Wager TT; Hou X; Verhoest PR; Villalobos A Moving beyond rules: the development of a central nervous system multiparameter optimization (CNS MPO) approach to enable alignment of druglike properties. ACS Chem. Neurosci 2010, 1, 435–449. [PubMed: 22778837]

(35). Rankovic Z CNS drug design: balancing physicochemical properties for optimal brain exposure. J. Med. Chem 2015, 58, 2584–2608. [PubMed: 25494650]

(36). Mikitsh JL; Chacko AM Pathways for Small Molecule Delivery to the Central Nervous System across the Blood-Brain Barrier. Perspect Medicin Chem., 2014, 6, 11–24. [PubMed: 24963272]

(37). Misra A; Ganesh S; Shahiwala A; Shah SP Drug delivery to the central nervous system: a review, J Pharm Pharm Sci. 2003, 6, 252–73. [PubMed: 12935438]

(38). Di L; Rong H; Feng B Demystifying brain penetration in central nervous system drug discovery. J. Med. Chem 2013, 56, 2–12. [PubMed: 23075026]

(39). Wager TT; Chandrasekaran RY; Hou X; Troutman MD; Verhoest PR; Villalobos A; Will Y Defining Desirable Central Nervous System Drug Space through the Alignment of Molecular Properties, in Vitro ADME, and Safety Attributes. ACS Chem. Neurosci, 2010, 1, 420–434. [PubMed: 22778836]

(40). Vasu D; Li H; Hardy CD; Poulos TL; Silverman RB 2-Aminopyridines with a Shortened Amino Sidechain as Potent, Selective, and Highly Permeable Human Neuronal Nitric Oxide Synthase Inhibitors, Bioorg. Med. Chem 2022, 69, 116878. [PubMed: 35772285]

(41). Kang S; Li H; Tang W; Martásek P; Roman LJ; Poulos TL; Silverman RB 2-Aminopyridines with a truncated side chain to improve human neuronal nitric oxide synthase inhibitory potency and selectivity. J. Med. Chem 2015, 58, 5548–5560. [PubMed: 26120733]

(42). Do HT; Wang H-Y; Li H; Chreifi G; Poulos TL; Silverman RB Improvement of Cell Permeability of Human Neuronal Nitric Oxide Synthase Inhibitors Using Potent and Selective 2-Aminopyridine-Based Scaffolds with a Fluorobenzene Linker. J. Med. Chem 2017, 60, 9360–9375. [PubMed: 29091437]

(43). Ji H; Stanton BZ; Igarashi J; Li H; Martásek P; Roman LJ; Poulos TL; Silverman RB Minimal pharmacophoric elements and fragment hopping, an approach directed at molecular diversity and isozyme selectivity. Design of selective neuronal nitric oxide synthase inhibitors. J. Am. Chem. Soc 2008, 130, 3900–3914. [PubMed: 18321097]

(44). Do HT; Li H; Chreifi G; Poulos TL; Silverman RB Optimization of Blood–Brain Barrier Permeability with Potent and Selective Human Neuronal Nitric Oxide Synthase Inhibitors Having a 2-Aminopyridine Scaffold. J. Med. Chem 2019, 62, 2690–2707. [PubMed: 30802056]

(45). Kang S; Tang W; Li H; Chreifi G; Martásek P; Roman LJ; Poulos TL; Silverman RB Nitric Oxide Synthase Inhibitors That Interact with Both Heme Propionate and Tetrahydrobiopterin Show High Isoform Selectivity. J. Med. Chem 2014, 57, 4382–4396. [PubMed: 24758147]

(46). Cinelli MA; Li H; Chreifi G; Poulos TL; Silverman RB Nitrile in the hole: discovery of a small auxiliary pocket in neuronal nitric oxide synthase leading to the development of potent and selective 2-aminoquinoline inhibitors. J. Med. Chem 2017, 60, 3958–3978. [PubMed: 28422508]

(47). Labby KJ; Xue F; Kraus JM; Ji H; Mataka J; Li H; Martásek P; Roman LJ; Poulos TL; Silverman RB Intramolecular hydrogen bonding: a potential strategy for more bioavailable inhibitors of neuronal nitric oxide synthase. Bioorg. Med. Chem 2012, 20, 2435–2443. [PubMed: 22370337]

(48). Xue F; Li H; Delker SL; Fang J; Martásek P; Roman LJ; Poulos TL; Silverman RB Potent, highly selective, and orally bioavailable gem-difluorinated monocationic inhibitors of neuronal nitric oxide synthase. J. Am. Chem. Soc 2010, 132, 14229–14238. [PubMed: 20843082]

(49). Silverman RB; Lawton GR; Ranaivo HR; Chico LK; Seo J; Watterson DM Effect of potential amine prodrugs of selective neuronal nitric oxide synthase inhibitors on blood–brain barrier penetration. Bioorg. Med. Chem 2009, 17, 7593–7605. [PubMed: 19796958]

(50). Wang H-Y; Qin Y; Li H; Roman LJ; Martásek P; Poulos TL; Silverman RB Potent and selective human neuronal nitric oxide synthase inhibition by optimization of the 2-aminopyridine based scaffold with a pyridine linker. J. Med. Chem 2016, 59, 4913–4925. [PubMed: 27050842]

(51). Ji H; Li H; Martasek P; Roman LJ; Poulos TL; Silverman RB Discovery of highly potent and selective inhibitors of neuronal nitric oxide synthase by fragment hopping. J. Med. Chem 2009, 52, 779–797. [PubMed: 19125620]

(52). Mannhold R; Kubinyi H; Folkers G Bioisosteres in Medicinal Chemistry, 2012, Vol. 54, Brown, ed., Wiley-VCH, Weinheim, Germany.

(53). Patani GA; LaVoie EJ Bioisosterism: A Rational Approach in Drug Design, Chem. Rev 1996, 96, 3147–3176. [PubMed: 11848856]

(54). Dick A; Cocklin S Bioisosteric Replacement as a Tool in Anti-HIV Drug Design, Pharmaceuticals, 2020, 13, 36; 10.3390/ph13030036. [PubMed: 32121077]

(55). Kosarych Z; Cohen T Rapid, high-yield cleavage of enol and dienol methyl ethers under mild conditions using chlorotrimethylsilane/sodium iodide, Tetrahedron Lett., 1980, 21, 3959–3962.

(56). Slaugh LH Lithium aluminum hydride, a homogeneous hydrogenation catalyst, Tetrahedron. 1966, 22, 1741–1746.

(57). Kowalski P; Majka Z; Kowalska T Acid-catalyzed *N*-debenzylation of benzylaminopyridines, Chem. Heterocycl. Compd, 1998, 34, 740–741.

(58). Zehnder L; Bennett M; Meng J; Huang B; Ninkovic S; Wang F; Braganza J; Tatlock J; Jewell T; Zhou J-Z; Burke B; Wang J; Maegley K; Mehta PP; Yin M-J Gajiwala KS; Hickey MJ; Yamazaki S; Smith E; Kang P; Sistla A; Dovalsantos E; Gehring MR; Kania R; Wythes M; Kung P-P Optimization of Potent, Selective, and Orally Bioavailable Pyrrolodinopyrimidine-Containing Inhibitors of Heat Shock Protein 90. Identification of Development Candidate 2-Amino-4-{4-chloro-2-[2-(4-fluoro-1*H*-pyrazol-1-yl)ethoxy]-6-methylphenyl}-*N*-(2,2-difluoropropyl)-5,7-dihydro-6*H*-pyrrolo[3,4-d]pyrimidine-6-carboxamide. J. Med. Chem 2011, 54, 3368–3385. [PubMed: 21438541]

(59). Williams AL; Dandepally SR; Kotturi SV A *p*-methoxybenzyl (PMB) protection/deprotection approach toward the synthesis of 5-phenoxy-4-chloro-*N*-(aryl/alkyl) thiophene-2-sulfonamides, Mol Divers, 2010, 14, 697–707. DOI 10.1007/s11030-009-9208-y. [PubMed: 19936959]

(60). Erdélyi M; Gogoll A Rapid Homogeneous-Phase Sonogashira Coupling Reactions Using Controlled Microwave Heating, J. Org. Chem, 2001, 66, 12, 4165–4169. [PubMed: 11397149]

(61). Hevel JM; Marletta MA [25] Nitric-oxide synthase assays. Methods Enzymol. 1994, 233, 250–258. [PubMed: 7516999]

(62). Di L; Kerns EH Drug-like properties: Concepts, structure design and methods: from ADME to Toxicity Optimization, 2nd Ed., Elsevier: Amsterdam, 2016; p 329.

(63). Jeffries B; Wang Z; Graton J; Holland SD; Brind T; Greenwood RDR; Le Questel J-Y; Scott JS; Chiarparin E; Linclau B Reducing the Lipophilicity of Perfluoroalkyl Groups by CF_2–F/CF_2–Me or CF_3/CH_3 Exchange, J. Med. Chem 2018, 61, 10602–10618. [PubMed: 30411895]

(64). Pennington LD; Moustakas DT The necessary nitrogen atom: a versatile high-impact design element for multiparameter optimization. J. Med. Chem 2017, 60, 3552–3579. [PubMed: 28177632]

(65). Mallo-Abreu A; Prieto-Díaz R; Jespers W; Azuaje J; Majellaro M; Velando C; García-Mera X; Caamaño O; Brea J; Loza MI; Gutiérrez-de-Terán H; Sotelo E Nitrogen-Walk Approach to Explore Bioisosteric Replacements in a Series of Potent A_{2B} Adenosine Receptor Antagonists, J. Med. Chem 2020, 63, 7721–7739. [PubMed: 32573250]

(66). Di L; Kerns EH; Fan K; McConnell OJ; Carter GT High throughput artificial membrane permeability assay for blood–brain barrier. Eur. J. Med. Chem 2003, 38, 223–232. [PubMed: 12667689]

(67). Davis TP; Sanchez-Covarubias L; Tome ME P-glycoprotein trafficking as a therapeutic target to optimize CNS drug delivery. Adv. Pharmacol 2014, 71, 25–44. [PubMed: 25307213]

(68). Löscher W; Potschka H Drug resistance in brain diseases and the role of drug efflux transporters. Nat. Rev. Neurosci 2005, 6, 591–602. [PubMed: 16025095]

(69). Patil AG; D'Souza R; Dixit N; Damre A Validation of quinidine as a probe substrate for the in vitro P-gp inhibition assay in Caco-2 cell monolayer. Eur. J. Drug Metab. Pharmacokinet 2011, 36, 115. [PubMed: 21725799]

(70). Hubatsch I; Ragnarsson EGE; Artursson P Determination of drug permeability and prediction of drug absorption in Caco-2 monolayers. Nat. Protoc 2007, 2, 2111–2119. [PubMed: 17853866]

(71). Csonka C; Pali T; Bencsik P; Gorbe A; Ferdinandy P; Csont T Measurement of NO in biological samples. Br. J. Pharmacol, 2015, 172, 1620–1632. [PubMed: 24990201]

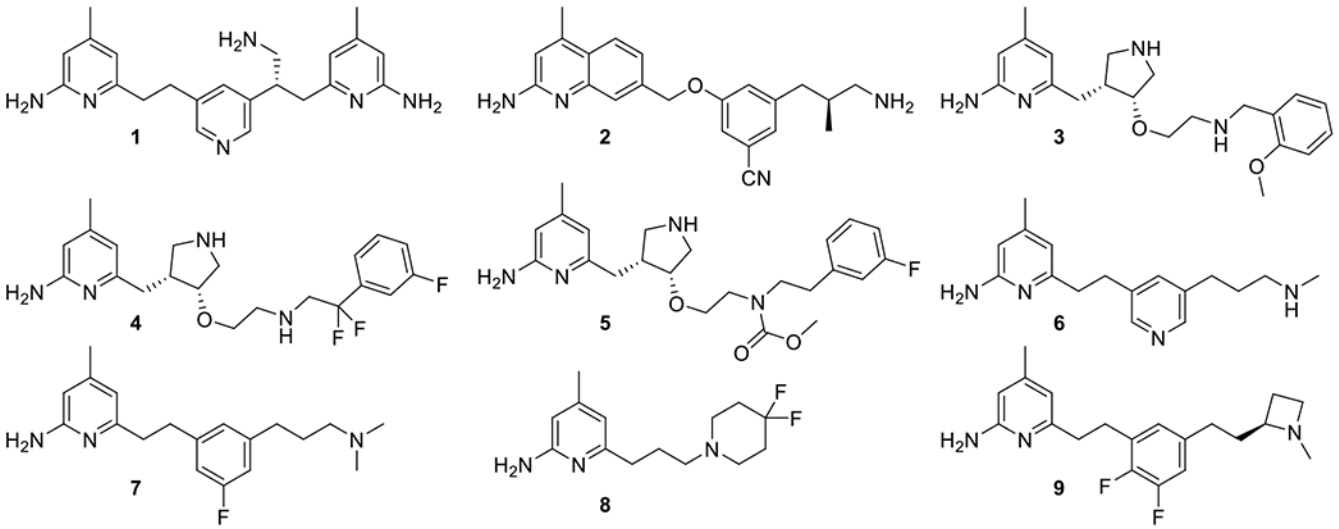

Figure 1.
Structures of recently described nNOS inhibitors

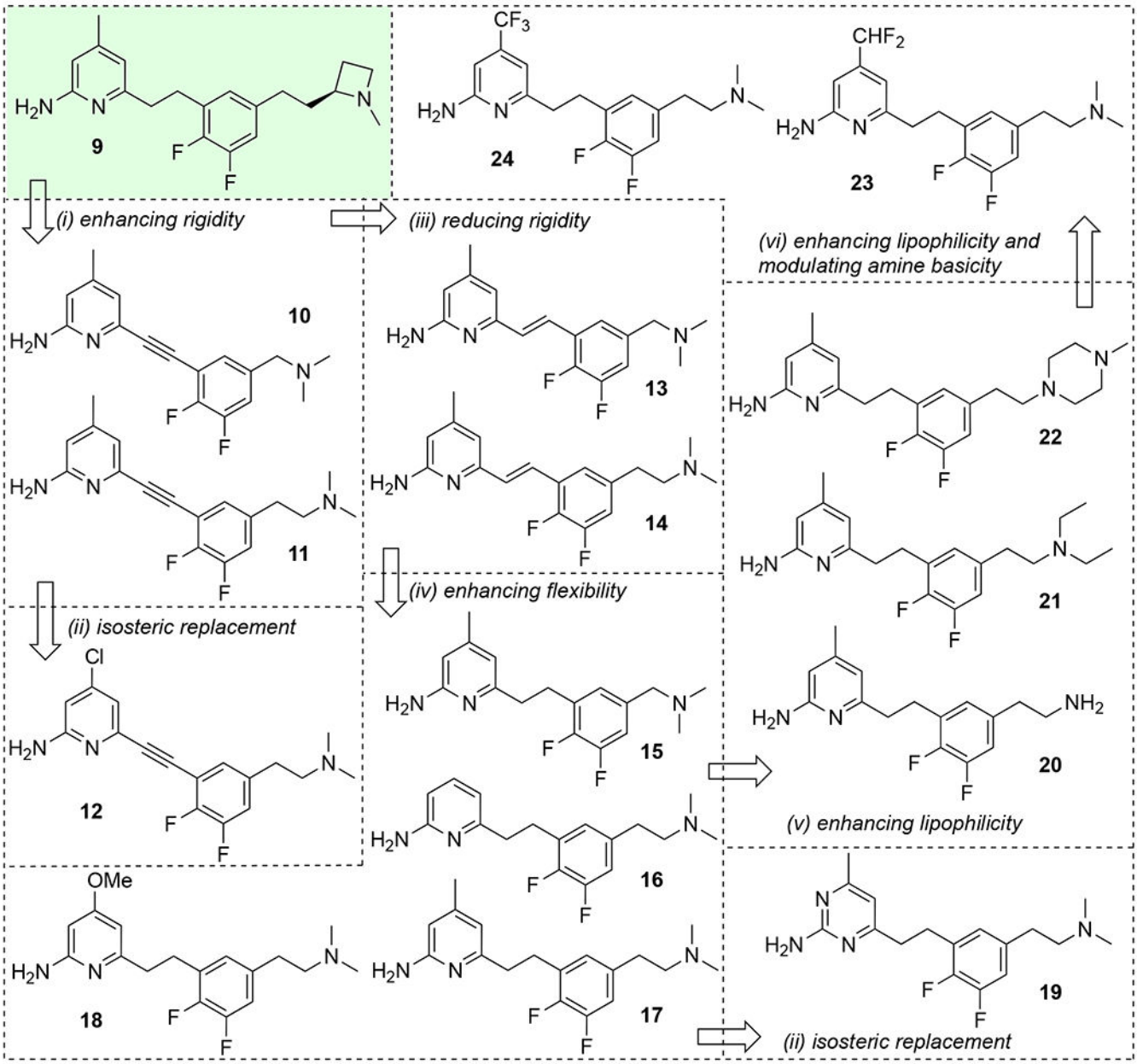

Figure 2.
Structural modification of lead **9**

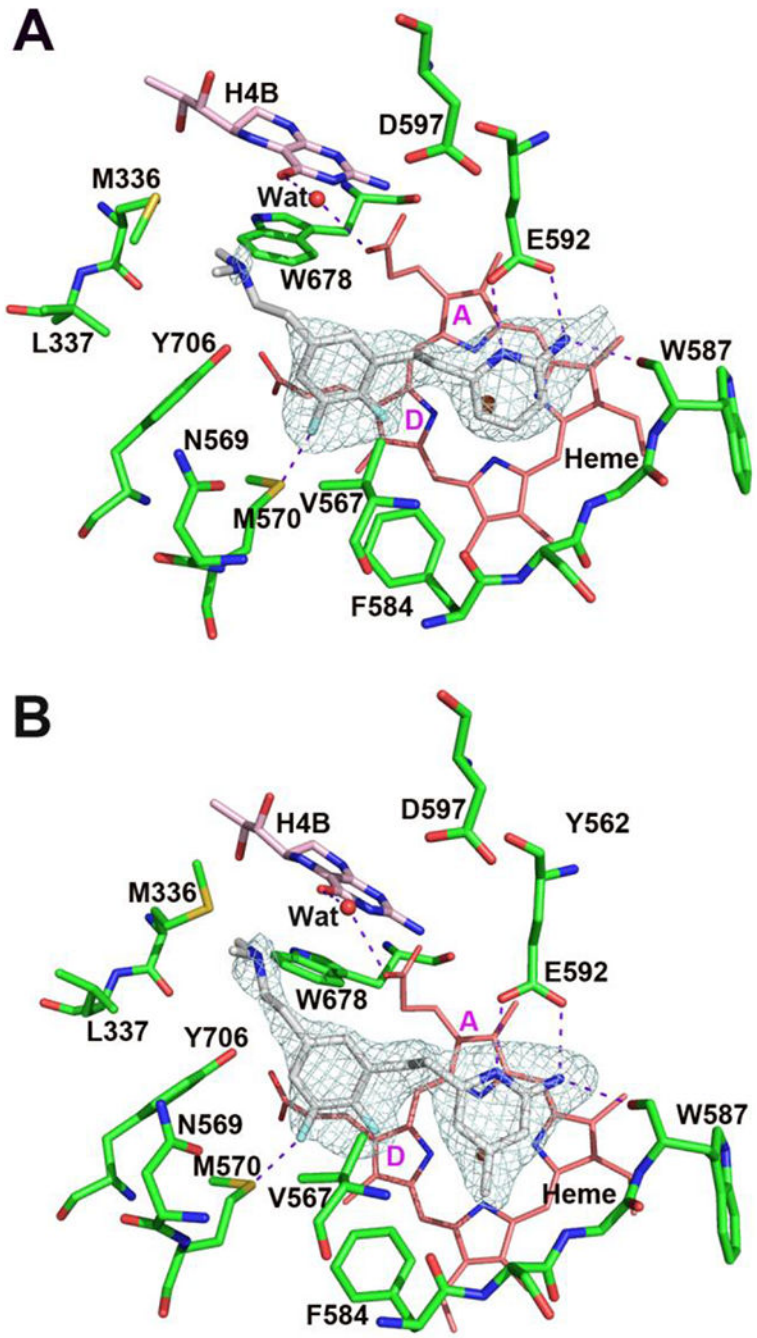

Figure 3.

Compound **16** (A, Protein Data Bank (PDB) code: 8FG9) or **17** (B, PDB code: 8FGA) bound in the active site of rnNOS. In this figure and all the following figures where crystal structures are reported, important hydrogen-bonds or other noncovalent bonds are depicted with dashed lines. Coloring of the backbone carbon atoms in rnNOS is green. The atomic color scheme for other atom types is: blue for nitrogen, red for oxygen, yellow-orange for sulfur, light-cyan for fluorine. The two heme propionates are labeled as A and D. The

electron density displayed around the inhibitor is the Fo-Fc omit difference map contoured at 3.0 σ calculated with the Polder routine in PHENIX.

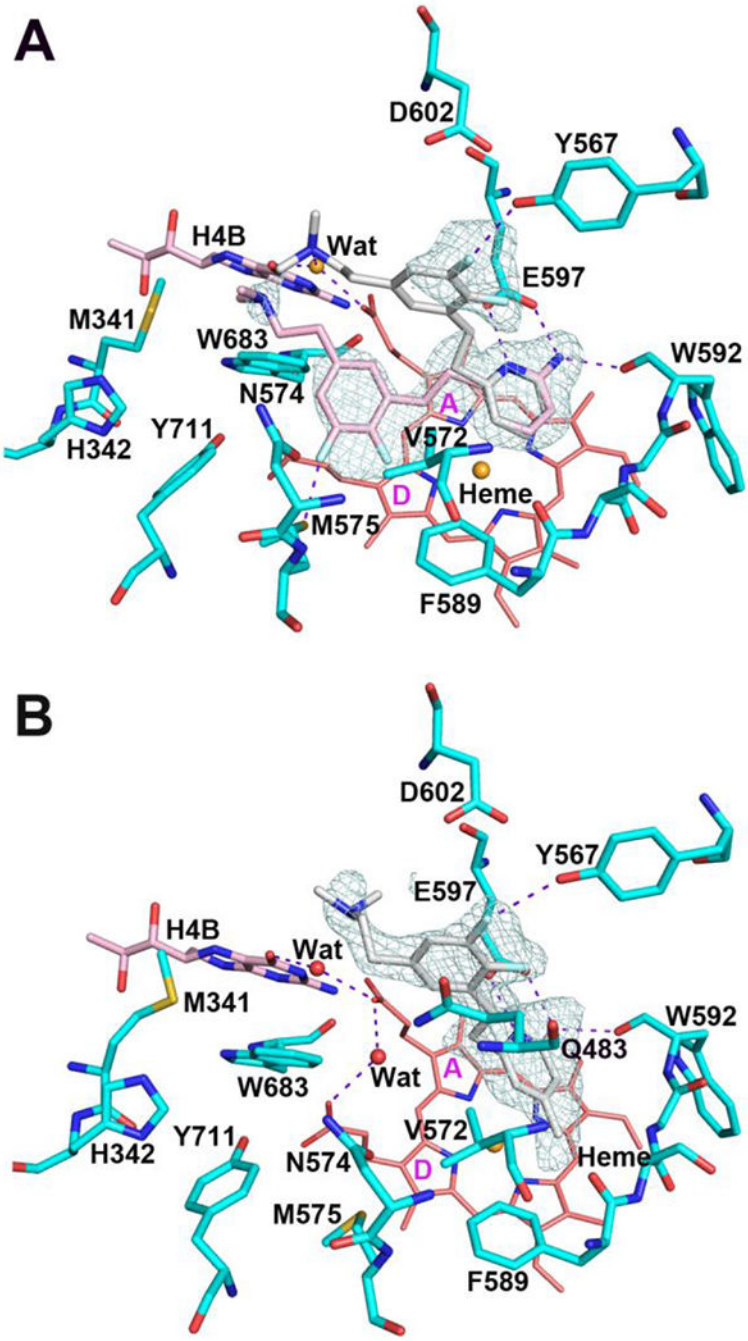

Figure 4.

Compound **16** (A, alternative inhibitor conformations, gray and light-pink, PDB code: 8FGF) or **17** (B, PDB code: 8FGG) bound to the active site of hnNOS. Coloring of the backbone carbon atoms in hnNOS is cyan.

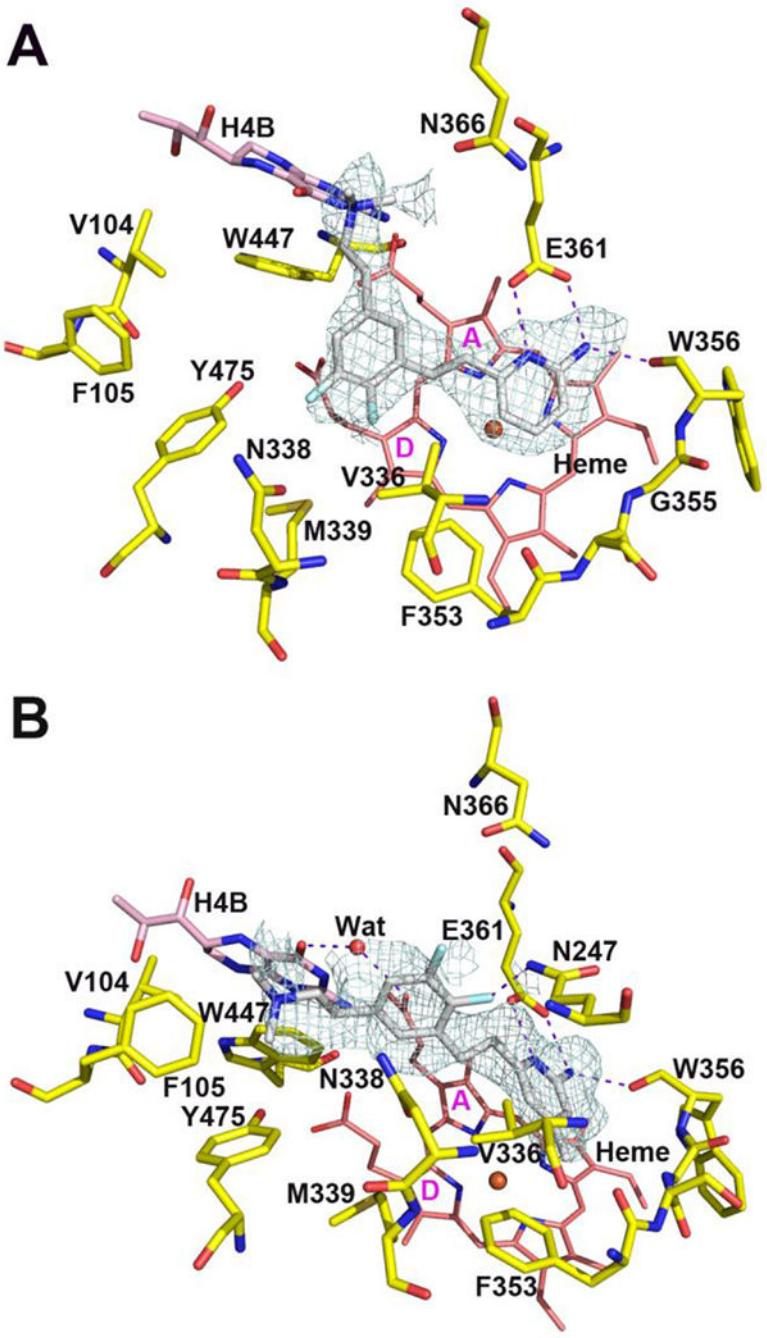

Figure 5.

Compound **16** (A, PDB code: 8FGN) or **17** (B, PDB code: 8FGO) bound to the active site of heNOS. Coloring of the backbone carbon atoms in heNOS is yellow.

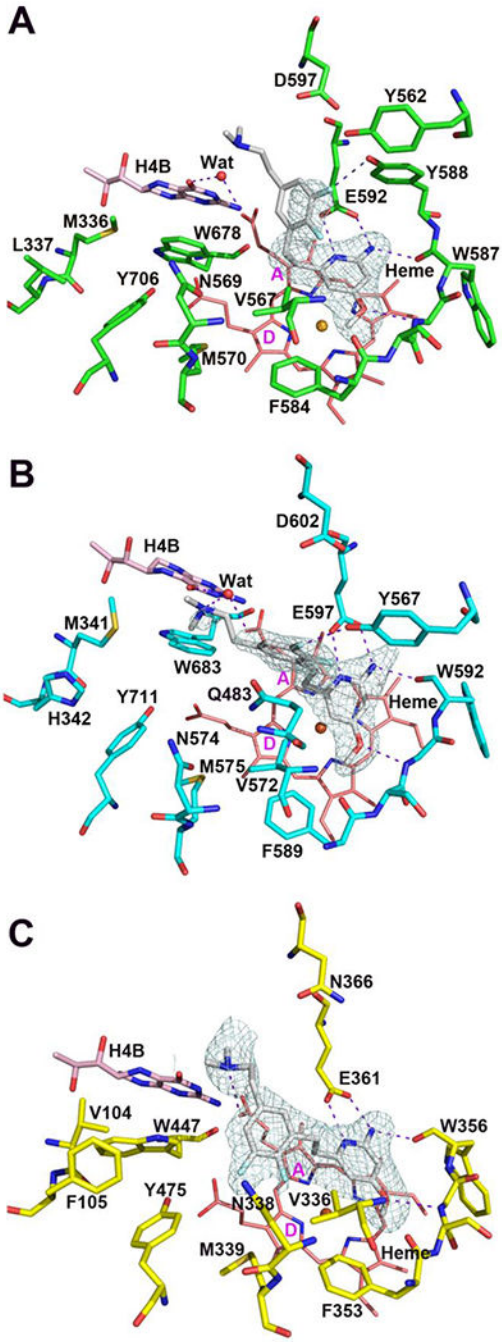

Figure 6.

Compound **18** bound to the active site of rnNOS (A, PDB code: 8FGV), hnNOS (B, PDB code: 8FGH), heNOS (C, PDB code: 8FGP).

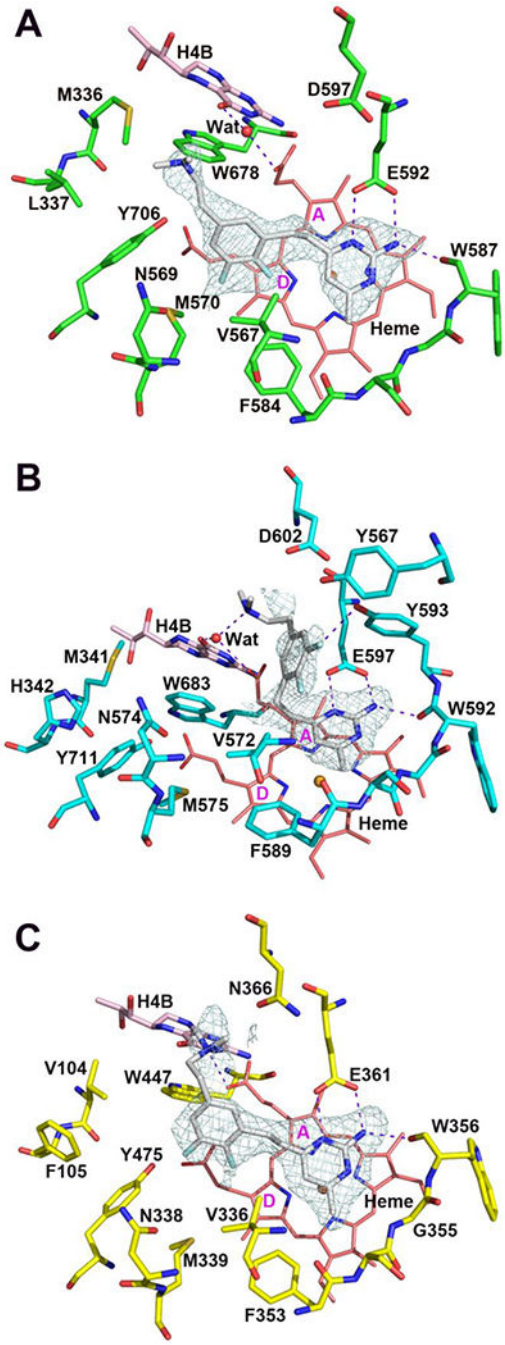

Figure 7.

Compound **19** bound to the active site of rnNOS (A, PDB code: 8FGB), hnNOS (B, PDB code: 8FGI), and heNOS (C, PDB code: 8FGQ).

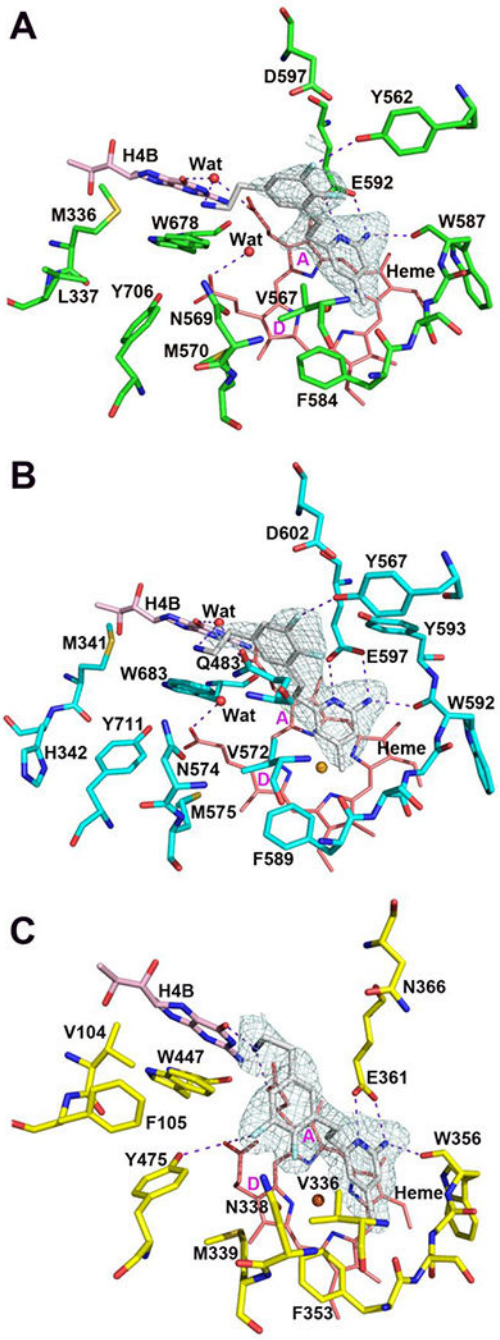

Figure 8.

Compound **20** bound to the active site of rnNOS (A, PDB code: 8FGC), hnNOS (B, PDB code: 8FGJ), and heNOS (C, PDB code: 8FGR).

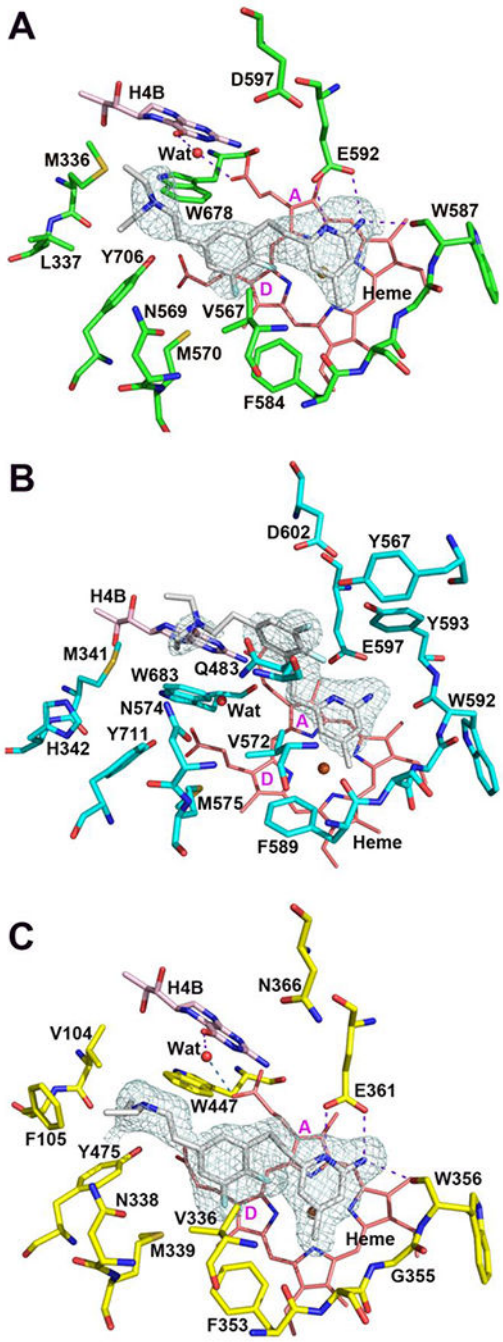

Figure 9.

Compound **21** bound to the active site of rnNOS (A, PDB code: 8FGD), hnNOS (B, PDB code: 8FGK), and heNOS (C, PDB code: 8FGS).

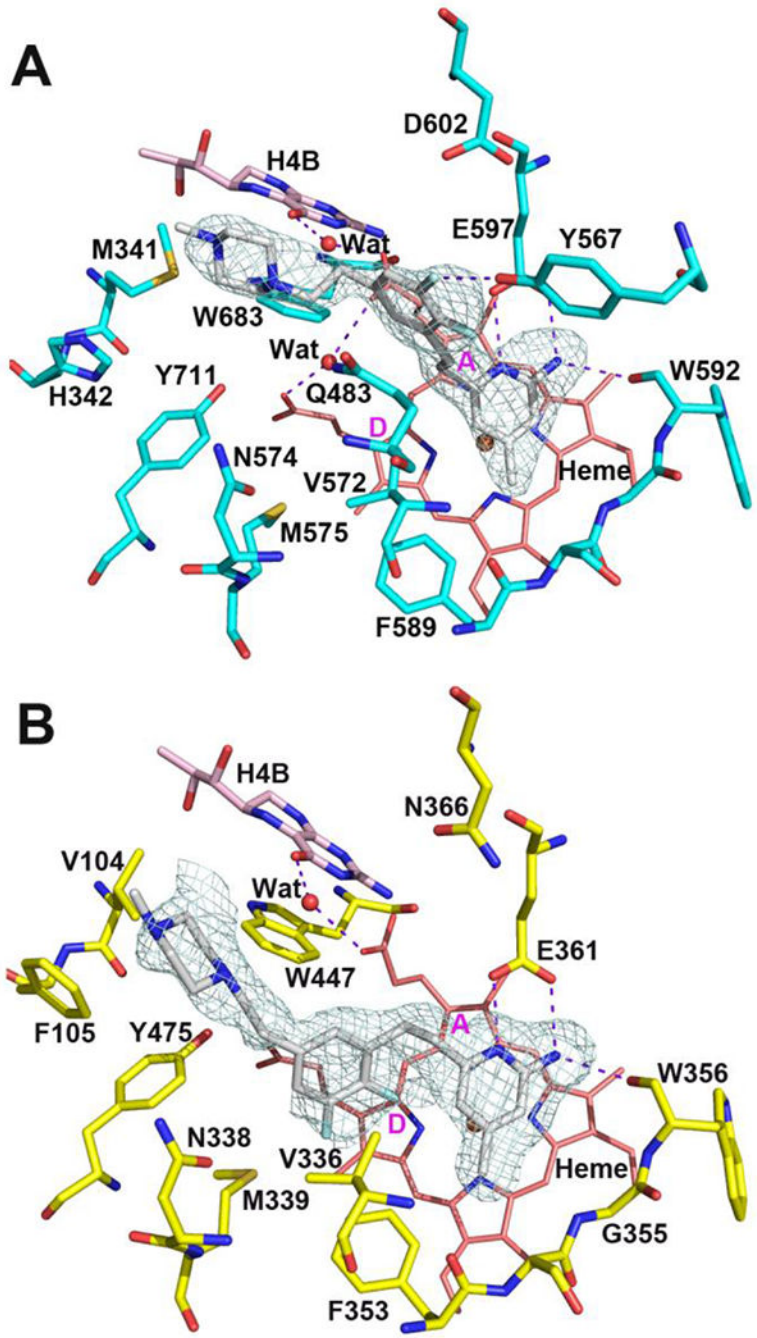

Figure 10.

Compound **22** bound to the active site of hnNOS (A, PDB code: 8FGL) and heNOS (B, PDB code: 8FGT).

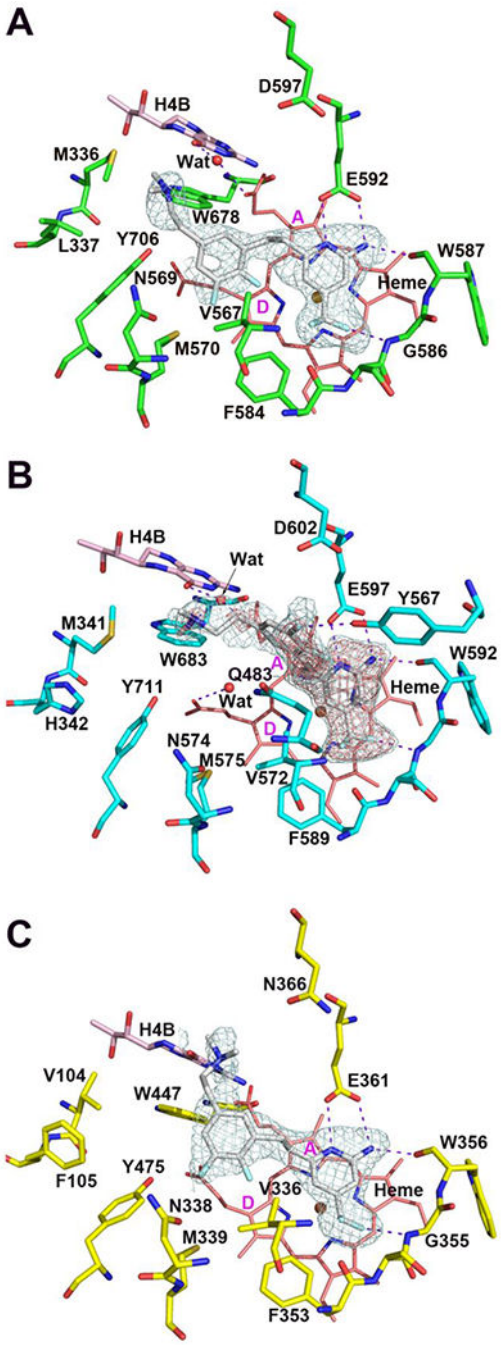

Figure 11.

Compound **23** bound to the active site of rnNOS (A, PDB code: 8FGE), hnNOS (B, PDB code: 8FGM), and heNOS (C, PDB code: 8FGU). In panel B, to show the support for an upward binding of **23**, the omit map has been contoured at both 3.0 σ (salmon) and 2.0 σ (pale cyan).

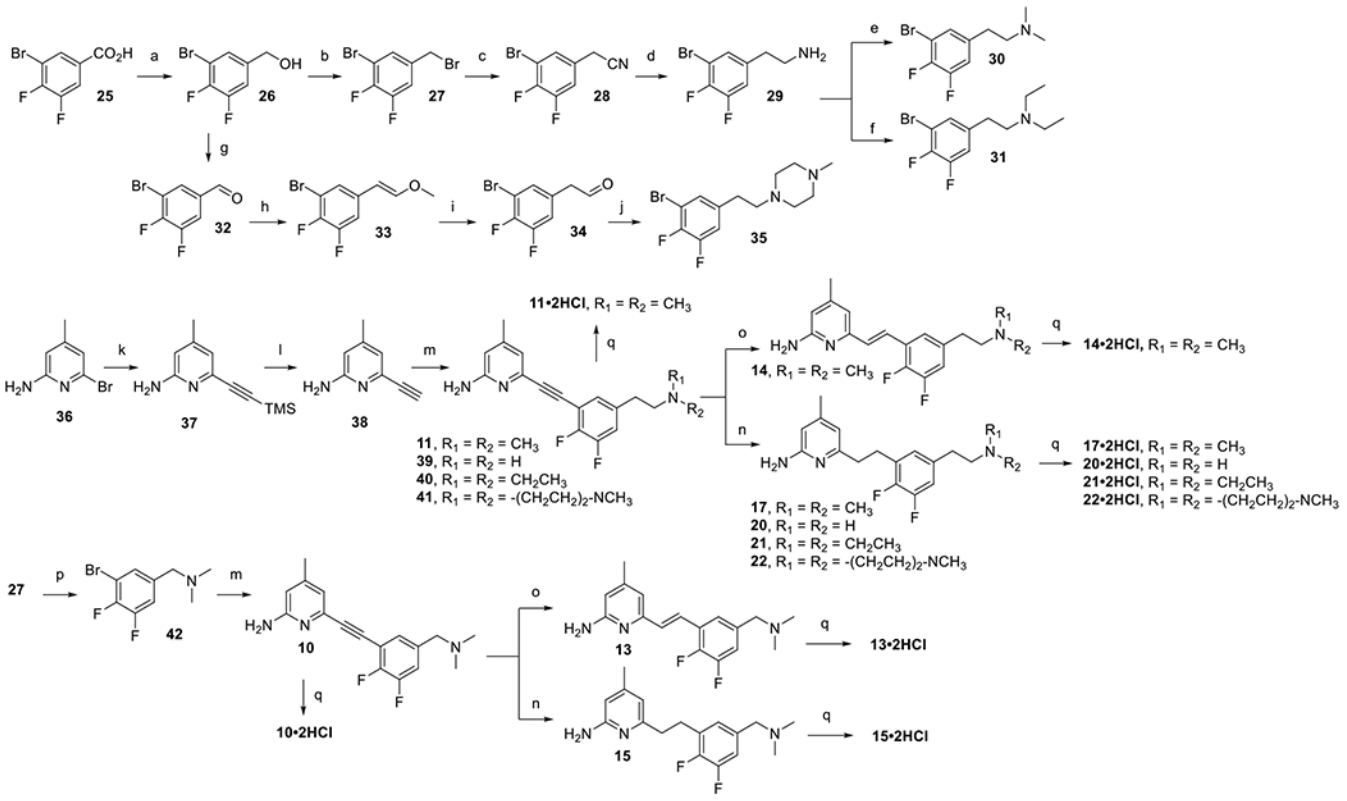

Scheme 1.[a]

Synthetic route to **10, 11**, **13-15**, **17**, and **20-22**

[a]Reagents and conditions: (a) BH_3•SMe_2, THF, 0 °C to 25 °C, 24 h; (b) CBr_4, PPh_3, 0 °C to 25 °C, 28 h, DCM; (c) KCN, (nBu)$_4$NBr, DCM:H_2O (1:1) (0.18 M), 24 h; (d) BH_3•SMe_2, THF, 0 °C to 25 °C, 30 h; (e) paraformaldehyde, $NaBH(OAc)_3$, CH_3CO_2H, 80 °C, 24 h; (f) acetaldehyde, $NaBH_3(CN)$, CH_3OH, 80 °C, 24 h; (g) DMSO, $(COCl)_2$, DCM, −78 °C, 30 min, and then **26**, −78 °C, 30 min, and then Et_3N, −78 °C to 25 °C, 2 h; (h) $CH_3OCH_2PPh_3Cl$, nBuLi, 0 °C, 30 min, and then **32**, 0 - 25 °C, 2 h; (i) TMSCl, KI, CH_3CN (0.05 M), 25 °C, 1 h (j) 1-methylpiperazine, $NaBH_3CN$, CH_3CO_2H, 80 °C, 1 h, 98%; (k) ethynyltrimethylsilane, $Pd(PPh_3)_4$, CuI, Et_3N, 120 °C, CH_3CN (0.12 M), 24 h; (l) K_2CO_3, CH_3OH:H_2O (20:1), 25 °C, 1 h; (m) **29-31**, **35**, and **42**, $PdCl_2$(dppf) or $Pd(PPh_3)_4$, CuI, Et_3N, 120 °C, CH_3CN (0.12 M), 12-24 h; (n) Pd/C, H_2, CH_3OH, 25 °C, 24 h; (o) $LiAlH_4$, THF, 40 °C, 5 h; (p) $(CH_3)_2NH$, Et_2O, 25 °C, 8 h; (q) HCl, CH_3OH, 0 °C-25 °C.

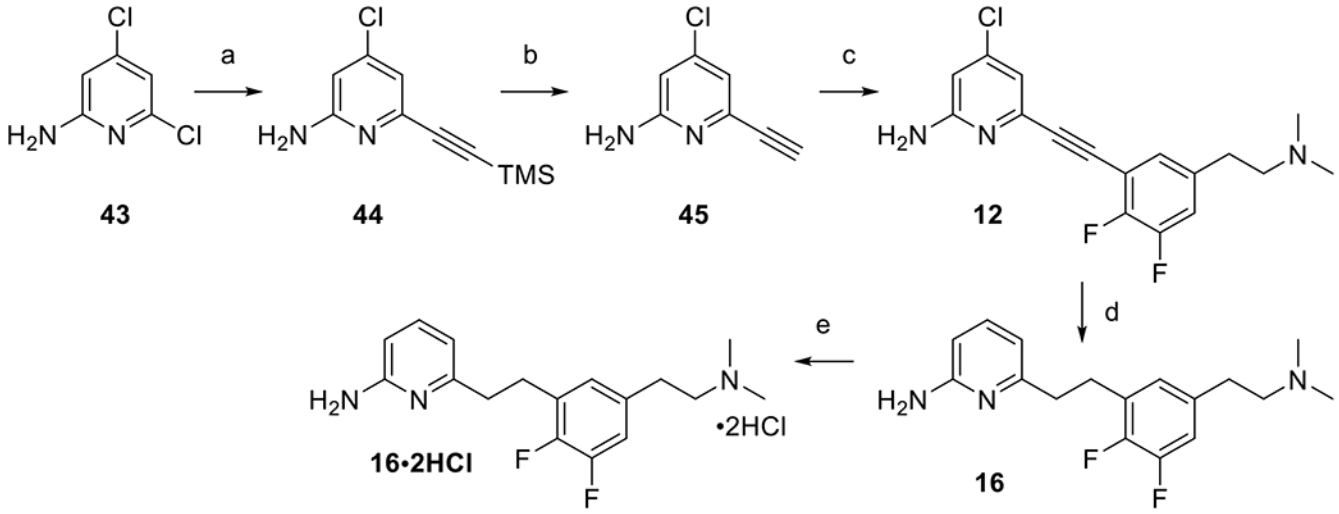

Scheme 2.[a]

Synthetic route to **12** and **16**

[a]Reagents and conditions: (a) Ethynyltrimethylsilane, $Pd(PPh_3)_4$, CuI, Et_3N, 120 °C, CH_3CN (0.12 M), 8 h; (b) K_2CO_3, CH_3OH:H_2O (20:1), 25 °C, 1 h; (c) **30**, $PdCl_2$(dppf), CuI, Et_3N, 120 °C, CH_3CN (0.12 M), 24 h; (d) Pd/C, H_2, CH_3OH, 25 °C, 2 h; (e) HCl, CH_3OH, 0 °C-25 °C.

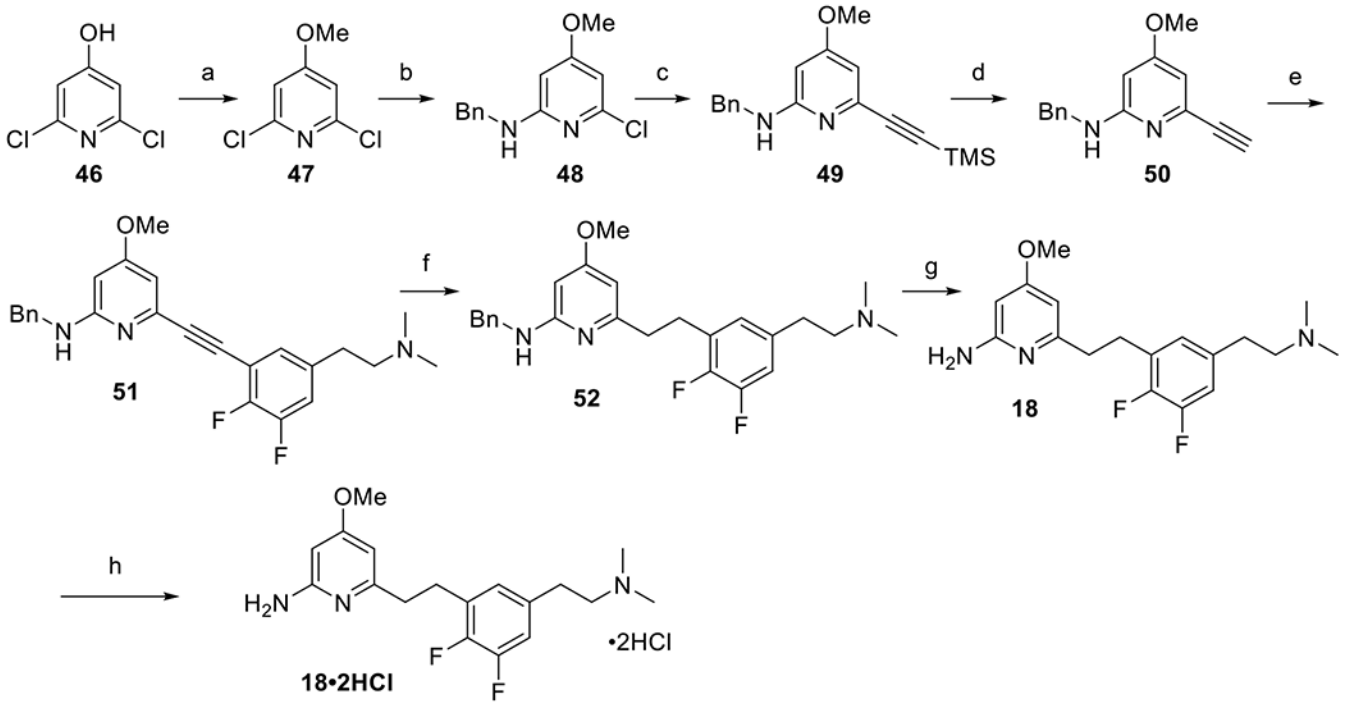

Scheme 3.[a]

Synthesis of **18**

[a]Reagents and conditions: (a) $(CH_3)_2SO_4$, K_2CO_3, THF, 90 °C, 16 h; (b) $PhCH_2NH_2$, K_2CO_3,150 °C, DMF, 2 h; (c) ethynyltrimethylsilane, $PdCl_2$(dppf), CuI, Et_3N, 120 °C, CH_3CN (0.23 M), 12 h; (d) K_2CO_3, CH_3OH:H_2O (20:1), 0.1 M, 25 °C, 30 min; (e) **30**, $PdCl_2$(dppf), CuI, Et_3N, 120 °C, CH_3CN (0.23 M), 16 h; (f) Pd/C, H_2, CH_3OH, 80 °C, 2 h; (g) Conc. H_2SO_4, 80 °C, 1 h; (h) HCl, CH_3OH, 0 °C-25 °C.

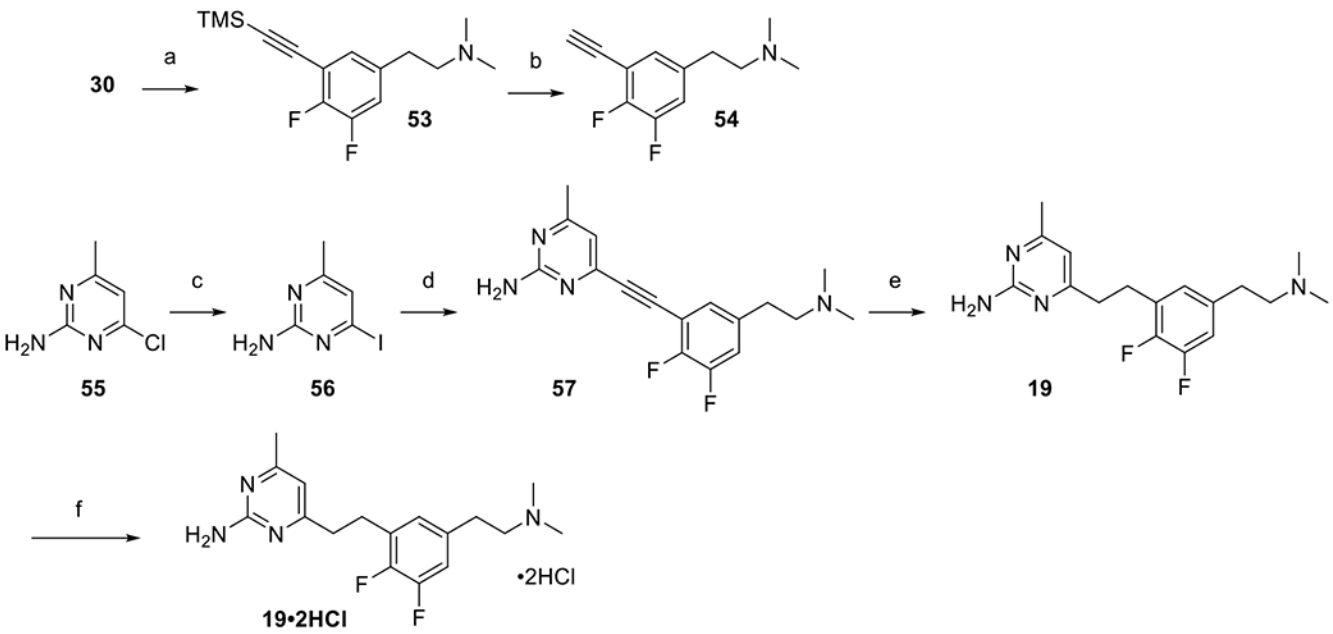

Scheme 4.[a]

Synthesis of **19**

[a]Reagents and conditions: (a) Ethynyltrimethylsilane, $PdCl_2$(dppf), CuI, Et_3N, 120 °C, CH_3CN (0.23 M), 16 h; (b) K_2CO_3, CH_3OH:H_2O (20:1), 0.1 M, 25 °C, 30 min; (c) TMSI, CH_3CN (0.17 M), 100 °C, 6 h; (d) **54**, $PdCl_2(PPh_3)_2$, CuI, Et_3N, 25 °C, CH_3CN (0.23 M), 4 h; (e) Pd/C, H_2, CH_3OH, 25 °C, 2 h; (f) HCl, CH_3OH, 0 °C-25 °C.

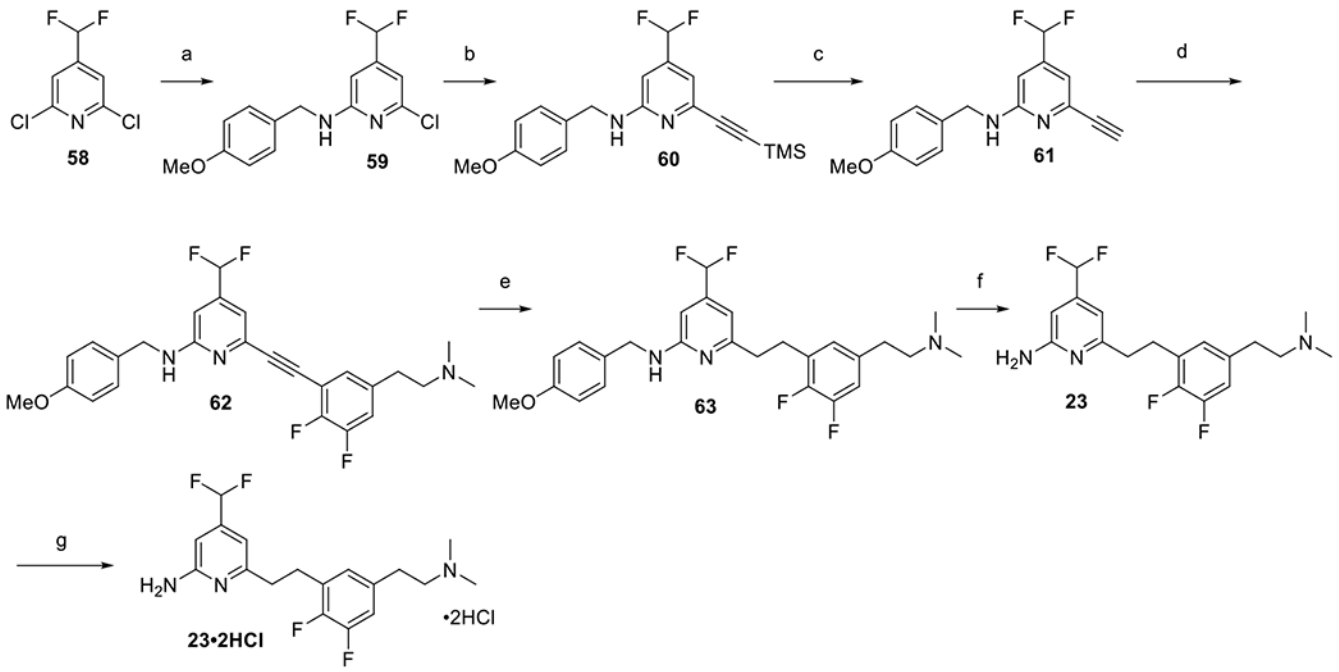

Scheme 5.[a]

Synthesis of **23**

[a]Reagents and conditions: (a) 4-Methoxybenzylamine, K_2CO_3, KI, *N*-methyl-2-pyrrolidone, 150 °C, 8 h; (b) ethynyltrimethylsilane, $PdCl_2(PPh_3)_2$, CuI, PPh_3, Et_3N, 120 °C, CH_3CN (0.23 M), 12 h; (c) K_2CO_3, CH_3OH:H_2O (20:1), 0.1 M, 25 °C, 30 min; (d) **30**, $PdCl_2$(dppf), CuI, Et_3N, 120 °C, CH_3CN (0.23 M), 24 h; (e) Pd/C, H_2, CH_3OH, 25 °C, 8 h; (f) TFA, DCM, 80 °C, 8 h; (g) HCl, CH_3OH, 0 °C-25 °C.

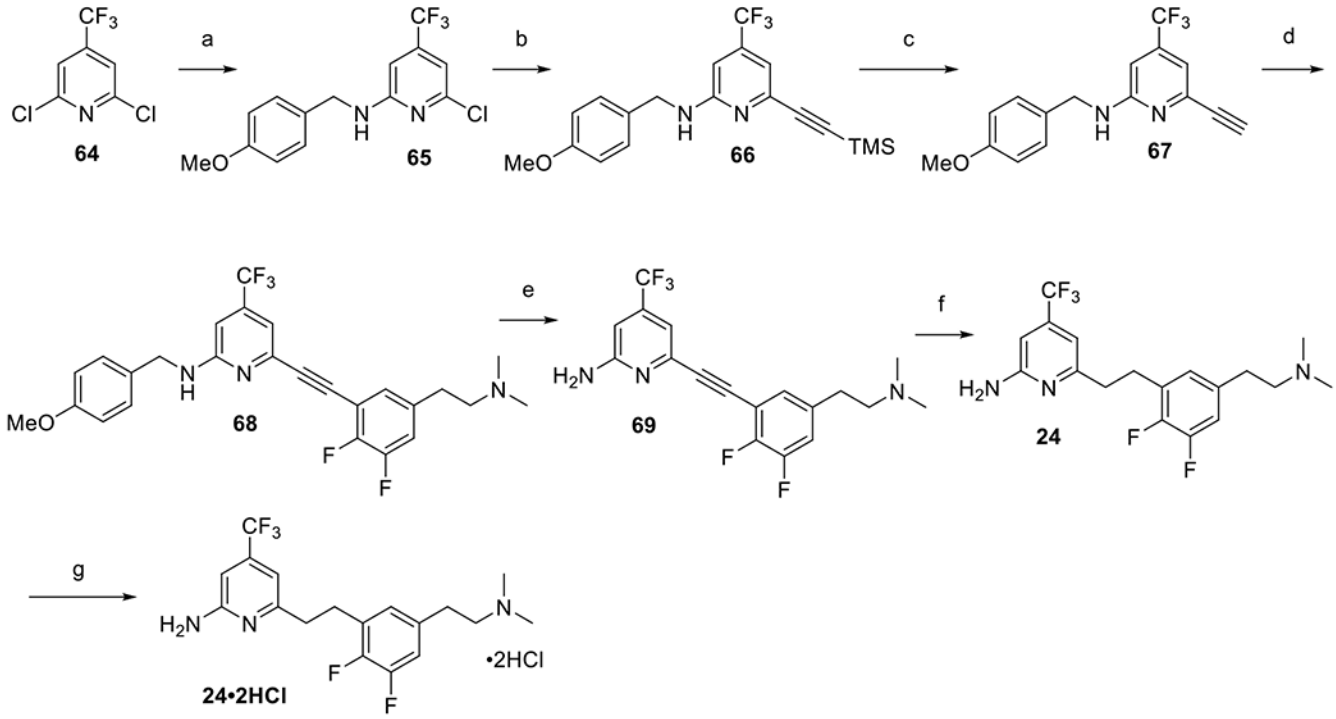

Scheme 6.[a]

Synthesis of **24**

[a]Reagents and conditions: (a) 4-Methoxybenzylamine, K_2CO_3, KI, *N*-methyl-2-pyrrolidone, 150 °C, 8 h; (b) ethynyltrimethylsilane, $PdCl_2(PPh_3)_2$, CuI, PPh_3, $(CH_3)_2NH$:DMF (1:1), 0.3 M, 120 °C, microwave, 20 min; (c) TBAF, THF, 0-25 °C, 30 min; (d) **30**, $PdCl_2(PPh_3)_2$, CuI, $(CH_3)_2NH$:DMF (1:1), 0.3 M, 120 °C, microwave, 20 min; (e) TFA, DCM, 80-100 °C, 15 min; (f) Pd/C, H_2, CH_3OH, 25 °C, 24 h; (g) HCl, CH_3OH, 0 °C-25 °C.

Table 1.

List of K_i values and selectivities of **10-24**

Compound	K_i (nM)[a]				Selectivity[b]		
	rat nNOS	human nNOS	human iNOS	human eNOS	hn/rn	hn/hi	hn/he
10 • 2HCl	392	319	88711	7676	0.8	278	24
11 • 2HCl	293	328	48844	18658	1.1	149	57
12 • 2HCl	1995	2417	65333	NT	1.2	27	NT
13 • 2HCl	129	NT	NT	NT	NT	NT	NT
14 • 2HCl	134	48	11893	14343	0.4	248	299
15 • 2HCl	91	NT	NT	NT	NT	NT	NT
16 • 2HCl	1108	1641	21116	61362	1.5	13	37
17 • 2HCl	**15**	**19**	**2181**	**20423**	**1.3**	**115**	**1075**
18 • 2HCl	75	55	4982	NT	0.7	91	NT
19 • 2HCl	6577	3833	39422	NT	0.6	10	NT
20 • 2HCl	60	81	1724	77158	1.4	21	953
21 • 2HCl	35	54	4212	46379	1.5	78	859
22 • 2HCl	83	89	10440	12415	1.1	117	139
23 • 2HCl	369	249	21476	NT	0.7	86	NT
24 • 2HCl	1313	2058	26316	68348	1.6	13	33

[a] K_i values were calculated from the IC_{50} values of the corresponding dose–response curves using the Cheng–Prusoff equation. For each compound, 8 to 11 concentrations were tested, and the IC_{50} value was calculated from an average of at least two duplicates. All standard errors were less than 10%.

[b] Selectivity values were determined by calculating the ratios of respective K_i values. The ratio hn/rn is desired to be as close to 1.0 as possible to avoid significant differences between rat and human dosages for clinical studies. For hn/hi and hn/he ratios, higher values are favorable.

NT = not tested.

Table 2.

Effective permeability (P_e) of five commercial drugs[66] and novel nNOS inhibitors in the PAMPA–BBB assay

Compounds	Reported P_e (10^{-6} cm s^{-1})[a]	Determined P_e (10^{-6} cm s^{-1})[b]	Prediction[c]
(±)-Verapamil	16	21.2 ± 0.43	CNS (+)
Desipramine	12	22.8 ± 0.93	CNS (+)
Chlorpromazine	6.5	10.8 ± 0.64	CNS (+)
Dopamine	0.2	0.13 ± 0.14	CNS (−)
Theophylline	0.12	0.1 ± 0.02	CNS (−)
10 • 2HCl		26.8 ± 0.64	CNS (+)
11 • 2HCl		15.7 ± 0.75	CNS (+)
12 • 2HCl		11.3 ± 0.49	CNS (+)
16 • 2HCl		11.5 ± 0.57	CNS (+)
17 • 2HCl		**13.7 ± 0.64**	**CNS (+)**
18 • 2HCl		6.8 ± 0.67	CNS (+)
19 • 2HCl		11.7 ± 1.83	CNS (+)
20 • 2HCl		12.6 ± 0.54	CNS (+)
21 • 2HCl		17.6 ± 0.18	CNS (+)
22 • 2HCl		10.4 ± 0.15	CNS (+)
23 • 2HCl		16.0 ± 1.54	CNS (+)
24 • 2HCl		17.3 ± 0.57	CNS (+)

[a] Reported effective permeability (P_e) values from the literature.[66]

[b] Effective permeability values were obtained in our in-house conditions. All assays were performed over 17 h at a concentration of 200 μM and tested in a triplicate for each compound.

[c] CNS (+) = likely high BBB permeation. CNS (−) = likely low BBB permeation. Note that the “predictions” for the five literature-based compounds listed have been experimentally tested.

Table 3.

Caco-2 apparent permeability and efflux ratio (ER) of selected nNOS inhibitors and control compounds

Compound	Apparent permeability (P_{app}, 10^{-6} cm s^{-1})[a]		Efflux ratio[e]
	mean A→B	mean B→A	
7 • 2HCl	9.2 ± 0.3	54.2 ± 17.6	5.9
9 • 2HCl	17.05 ± 0.08	13.71 ± 0.07	0.8
17 • 2HCl	24.92 ± 0.07	12.03 ± 0.09	0.48
Metoprolol[b]	37.18	20.39	0.55
Atenolol[c]	0.39	0.58	1.47
Erythromycin[d]	<0.17	13.39	>78.76

[a] All assays were performed over 2 h at a concentration of 10 μM. Apparent permeability was measured for each compound in duplicate using a Caco-2 bidirectional permeability assay[70]

[b] High permeability control.

[c] Low permeability control.

[d] High efflux control.

[e] Efflux ratio is defined as P_{app} (B → A)/P_{app} (A → B); efflux ratio values >3 indicate that a compound may be a substrate for P-gp or other active transport systems.

Table 4.

Metabolic stability of nNOS inhibitors in mouse and human liver microsomes

Compound	Half-life ($t_{1/2}$, min)	
	MLM	HLM
Terfenadine	-	15
Imipramine	9	-
9 • 2HCl	16	> 60
17 • 2HCl	29	> 60